

**1 Simulation of surface and top of atmosphere thermal**  
**2 fluxes**  
**3 and radiances from the RADAGAST experiment**

N.A. Bharmal, A. Slingo, G.J. Robinson, J.J. Settle

4 Environmental Systems Science Centre, University of Reading,

5 Whiteknights, Reading RG6 6AL, United Kingdom

---

**Abstract.**

Simultaneous observations of thermal radiative fluxes and radiances, from the surface (ARM Mobile Facility, Niamey) and top of atmosphere (Geostationary Earth Radiation Budget instrument), during the RADAGAST experiment are compared with results from a radiative transfer model (Edwards-Slingo). Emphasis is placed on diagnosing the accuracy of the cloud-free radiation measurements using multiple instruments at the surface, and thus independently establishing the magnitudes of the aerosol direct effect. It is found that the surface forcing from aerosol regularly exceeds  $20 \text{ Wm}^{-2}$ , and reached  $\sim 100 \text{ Wm}^{-2}$  during the March 2006 dust storm. Equivalent comparisons are made with top of atmosphere measurements, and radiance-closure is achieved. As the fluxes at top of atmosphere are a product retrieved from the radiances, it is not surprising that significant discrepancies are found between these product fluxes and the simulated values. Using the simulated radiance-to-flux conversion, with the measured radiances, a hybrid top of atmosphere outgoing longwave flux is created as an alternative to the GERB product. At 11 UT (local noon), this hybrid differs from the product by  $\sim 5 - 15 \text{ Wm}^{-2}$  depending on time of year and aerosol loading. Combining the observations and simulations (including the hybrid OLR), or using either alone, the longwave clear sky atmospheric heating (divergence) is derived. Differences of  $\sim 10\%$  between the three alternatives are found, but all agree as to the diurnal variability being the time period with the largest amplitude fluctuations when cloud is not present.

## 1. INTRODUCTION

29 North Africa and the Arabian peninsula share one of the most unusual radiation en-  
30 vironments on the planet. For example, this is the only tropical region with a negative  
31 annual-mean net radiation balance at the top of the atmosphere [*Hartmann, 1994*]. There  
32 are few, permanent surface radiation measurement sites [*Ohmura et al., 1998*], in part  
33 because of the harsh environment. In addition, until recently, broadband radiation bud-  
34 get measurements at the top of the atmosphere (TOA) were limited to twice per day,  
35 from instruments on sun-synchronous platforms [*Jacobowitz et al., 1984; Barkstrom, 1984;*  
36 *Hucek et al., 1996*]. The launch of the Geostationary Earth Radiation Budget (GERB)  
37 instrument [*Harries et al., 2005*] in 2002 substantially improved the TOA sampling. The  
38 deployment of the Atmospheric Radiation Measurement (ARM) Program Mobile Facility  
39 (AMF) to Niamey, Niger for 2006 [*Miller and Slingo, 2007*] provided a similar improvement  
40 in surface sampling. The combination of GERB and the AMF within the RADAGAST  
41 experiment, [*Slingo et al., 2008a*] has resulted in a year-long time series of shortwave and  
42 longwave radiation measurements from both surface and TOA, together with associated  
43 meteorological variables.

44 These observational developments provide an opportunity to test radiative transfer  
45 schemes within this environment. In turn, the simulations can be used to examine the  
46 consistency of the measurements and to arrive at an improved representation of the over-  
47 all radiation budget. This work represents a first step in this process, by concerning  
48 itself with simulations of the longwave fluxes and divergences. The Sahelian location of  
49 Niamey is interesting from a modeling perspective for several reasons; in particular, the

50 range of integrated column water vapor (CWV) and aerosol optical depth. Both are con-  
51 sequences of the location, which causes Niamey to be affected by the moist southwesterly  
52 winds of the West African monsoon in boreal summer, and by the dry, and dust laden,  
53 northeasterly Harmattan winds from the Sahara in boreal winter.

54 The geostationary orbit of the GERB instrument allows for  $\sim 15$  minute sampling of  
55 the diurnal radiances at TOA. This resolution is matched by observations at the AMF,  
56 thus making comparisons with radiative transfer simulations relatively straightforward.  
57 To derive the atmospheric heating, it is possible simply to combine the observations from  
58 the surface and TOA [*Slingo et al.*, 2008b]. However, this is strictly only valid if the  
59 measurements have identical spatial scales. The consequence of using this assumption is  
60 studied here. The principle difficulty is that the surface measurements are made from  
61 a single point, whereas the satellite data are integrated over the ‘footprint’ (the point  
62 spread function) of the instrument. This mismatch in spatial scales can result in radiative  
63 inconsistencies—such as in the description of the land surface or of cloudiness—which,  
64 in turn results in increased random and systematic errors. The random error effect is  
65 analyzed in a companion paper [*Settle et al.*, 2008] and is ignored here by assuming  
66 atmospheric homogeneity and surface stationarity. The systematic errors are studied and  
67 reduced by using satellite retrievals to characterize the wider area about the AMF.

68 This paper utilizes clear-sky conditions, partly to satisfy the sky homogeneity assump-  
69 tion. The aim is to establish the uncertainties and biases in the cloud-free simulations,  
70 which are important in subsequently quantifying radiation closure errors when clouds are  
71 present. By using a cloud mask to screen out cloud effects, the coverage of the radi-  
72 ation observations is decreased by  $\sim 20\%$  during the dry season and  $\sim 66\%$  during the

73 wet (monsoon) season. (These seasons are of approximately the same length, and the  
74 monsoon period is defined for 2006 [*Slingo et al.*, 2008a] as being between May 5th and  
75 October 29th inclusive.)

76 In the longwave, the aerosol direct effect at the surface varies greatly, depending on  
77 region and the nature of the transported particles [*Claquin et al.*, 1998; *Miller et al.*, 2004;  
78 *Ritter et al.*, 2005; *Dey and Tripathi*, 2008], between  $\sim 1$  and  $\sim 70 \text{ Wm}^{-2}$ . The upper limit  
79 quoted here was found from simulations with desert-like atmospheric & surface conditions  
80 and dust particle radii greater than  $1 \mu\text{m}$ . Since there is a paucity of radiation studies  
81 within such environments—which do occur during RADAGAST [*Slingo et al.*, 2006]—the  
82 full range of direct effect values is expected here. This variation will be exploited in this  
83 paper to understand the aerosol direct effect via correlations with visible retrievals: surface  
84 infra-red retrievals [*Turner*, 2008] may be biased for the same reason as the aerosol-free  
85 simulations, which allows for a consistent surface flux closure at the surface, but will then  
86 cause erroneous TOA flux closure. Note that as TOA fluxes are retrievals themselves, it  
87 is necessary to study their accuracy under conditions where aerosol is present.

88 In the following section, the measurements of, and arrangements for modeling, the long-  
89 wave radiation during 2006 at Niamey are introduced, as well as the data that are used  
90 to represent the disparity in spatial scales between the surface and TOA data. Section 3  
91 analyzes simulations of aerosol-free fluxes at the surface, with the emphasis on diagnosing  
92 the accuracy of the humidity profile used in the radiative transfer code. A comparison is  
93 also made with zenith radiances observed at the surface in several wavebands. The pre-  
94 sumed aerosol-direct effect from surface flux measurements and simulations is compared  
95 with aerosol retrievals. Having established the magnitude of the aerosol direct effect at

96 the surface, the radiances and fluxes at the TOA are compared in Section 4. The GERB  
97 radiance-to-flux conversion is studied, in order to quantify what causes the differences  
98 that are found between the simulated fluxes and GERB observations. The simulated di-  
99 rect aerosol effect is used to determine an aerosol loading and the comparison of TOA  
100 radiances and fluxes is repeated with the simple aerosol representation. From the pre-  
101 vious two sections, the flux components required for atmospheric heating (divergence)  
102 calculations have been analysed and summarised as a best-estimate collection. Section 5  
103 presents estimates of the cloud-free divergence from this flux collection, and compares the  
104 results to the same from observed fluxes only (c.f. *Slingo et al.* [2008b]) and simulated  
105 fluxes only. The conclusion summarizes the results and suggests further studies using the  
106 dataset.

## 2. BACKGROUND

### 2.1. Radiation measurements

107 The RADAGAST field experiment consisted of two primary measurement locations, the  
108 ARM Mobile Facility (AMF) [*Miller and Slingo, 2007*] and the Geostationary Earth Ra-  
109 diation Budget instrument aboard Meteosat-8. The AMF was located at Niamey airport  
110 ( $2.18^\circ$  E,  $13.48^\circ$  N) and was present between mid-December 2005 and early-January 2007:  
111 data relevant to this work range from 6th January to 31st December. The GERB instru-  
112 ment (GERB-2) was, throughout this period, located above  $3.3^\circ$  W,  $0.0^\circ$  N. The AMF was  
113 active for each day of 2006, with short instrumental dropouts, whilst GERB suffered from  
114 only two outages longer than a day. (Notably, the GERB instrument is taken offline into  
115 sun-avoidance mode during 4 hours about midnight for 110 days.)

116 The measurements of the downwelling surface thermal radiation are from two sources:  
117 broadband fluxes from a pyrgeometer (using one of the two instruments), and spectral  
118 zenith radiances from the AERI spectrometer [*Knuteson et al.*, 2004]. A distinct advantage  
119 of the AERI is its continuous calibration sequence, scheduled between measurements of  
120 sky radiation, which results in known measurement characteristics for all times. The  
121 rawinsonde ascents were made four times daily at times described as 06 UT, 11 UT 17 UT,  
122 and 23 UT. (Restricting sonde data to those launched within 1 hr of these times removed  
123 4 % of the launches.) These data were all retrieved from the ARM archive and those used  
124 in this work are presented in table 1. The more physically accurate MWRRET [*Turner*  
125 *et al.*, 2007] measurements of CWV replaced the MWRLOS data stream. In addition,  
126 using AMF observations alone, a surface-based cloud mask was created, analogous to  
127 other worker's approaches [*Henderson*, 2006; *Long and Ackerman*, 2000].

128 The GERB [*Harries et al.*, 2005] instruments measure the total and shortwave radiance  
129 from geostationary orbit, and their difference returns the longwave radiance. A conversion  
130 process for the longwave [*Clerboux et al.*, 2003] produces the associated flux products. In  
131 this work, the Edition 1 ARG products [*Dewitte et al.*, 2008] are used. Also aboard the  
132 Meteosat platform is the SEVIRI spectral imager [*Schmetz et al.*, 2002], whose measure-  
133 ments contribute toward two purposes in this work. First, a GERB-SEVIRI product of  
134 broadband radiances and fluxes, the SHI product, is a second estimate of radiation at ap-  
135 proximately 5 times higher resolution than the ARG product but at identical measurement  
136 times. Second, the SEVIRI radiances are used by NWCSAF [*Slingo et al.*, 2008b; *Derrien*  
137 *and Le Gleau*, 2005] to produce a TOA cloud-mask. These products are summarised in  
138 table 2.

139 The errors from radiative measurements are provided in two different fashions: for the  
140 surface measurements, a standard deviation is made from the 60 samples per minute,  
141 whilst for the GERB ARG and SHI products, the quoted error for the radiances is a  
142 relative value and there is an additional error for the fluxes . These are summarised in  
143 *Slingo et al.* [2006] as  $\pm 5 \text{ Wm}^{-2}$  for the surface fluxes, 1 % for the GERB radiances, and  
144  $\sim 5 \text{ Wm}^{-2}$  for the GERB fluxes.

## 2.2. Tools & other measurements

145 The radiative transfer calculations were made using the Edwards-Slingo code (hence-  
146 forth ES96) [*Edwards and Slingo*, 1996]. Despite being designed for computational effi-  
147 ciency, it remains flexible in several areas which are useful in this work e.g. either 2-stream  
148 or spherical harmonic solvers are available for fast calculation of both fluxes and radiances.  
149 The optical parameters of gases and aerosols are specified via spectral files, and here the  
150 spectral file is as used in the MetOffice HadGEM1 model [*Martin et al.*, 2006]. In par-  
151 ticular, the aerosol specification in this file is from the WMO [WMO/TD-No. 411] with  
152 a modified size distribution [*d'Almeida et al.*, 1991]. Using the times of sonde launches  
153 restricts the calculations to 4 per day, but this is sufficient to resolve the diurnal cycle for  
154 this work.

155 A (binary) cloud mask is used to remove the times in the measurements when cloud  
156 affects the radiation. The SEVIRI-NWCSAF cloud mask results in  $\sim 270$  values per  
157 GERB ARG pixel, whose average when greater than 0.1 is interpreted as cloud. This  
158 mask results in evident false negatives from the surface perspective, therefore the surface-  
159 based cloud mask replaces it for surface comparisons. However, when combining TOA and

160 surface fluxes for divergence estimates, a joint mask is produced by assuming independence  
161 of each mask and combining them via a Boolean OR operator.

162 The radiative transfer inputs are obtained from sonde data to produce the temperature  
163 and humidity profiles. The humidity is then scaled [*Soden et al.*, 2004] such that it  
164 produces a CWV which is equal to the value from MWRRET retrievals. The profiles  
165 have  $\sim 150$  pressure levels with a standard ozone prescription [*Ellingson et al.*, 1991], and  
166 the long-lived gas species ( $\text{CO}_2$ ,  $\text{CH}_4$ ,  $\text{O}_2$ ,  $\text{N}_2\text{O}$ ) have vertically constant mixing ratios  
167 consistent with values from 2005. (All halocarbons are neglected.)

168 The profiles can be used to simulate pristine sky (aerosol- & cloud-free) radiation fields,  
169 and then, by comparisons with measurements, an estimate can be made of the direct  
170 radiative effect of aerosols. A companion paper in this special section concerning infra-  
171 red aerosol retrievals, from AERI radiances [*Turner*, 2008], shows good agreement of  
172 11 micron optical depths with 1 micron AERONET retrievals from Banizoumbou [*Holben*  
173 *et al.*, 2001],  $\sim 60$  km east of Niamey. (The AERONET site at Niamey itself only operated  
174 from August 2006 onwards.) The analysis showed that a reasonable assumption is for the  
175 Ångstrom exponent between 11 microns and 1 micron to be a constant ( $\sim 0.33$ ). As a  
176 result, the Banizoumbou AERONET retrievals will be used here as a proxy for IR optical  
177 depths.

178 The airport location means the area underneath the AMF radiation instruments is  
179 unrepresentative of the larger GERB ARG footprint. In particular, the wider area includes  
180 the River Niger and the urban area of Niamey proper. Hence, the profile infra-red surface  
181 properties—emissivity and surface temperature (LST)—use both satellite retrievals and  
182 AMF measurements. The retrievals are from the MODIS instruments: temperature (LST)

183 via the MOD11A2 & MYD11A2 products [*Wan and Li*, 1997], and emissivity via the  
184 CIMMS IR emissivity database [*Seemann et al.*, 2008].

185 The CIMMS emissivities are estimates for several narrow bands over the longwave spec-  
186 trum. They are provided as month-long averages with  $0.05^\circ$  spatial resolution. From these  
187 emissivities, the broadband emissivity was derived via two approaches: by a bandwidth-  
188 weighted average and by using pre-determined weightings [*Wang et al.*, 2005]. Averaged  
189 over the GERB ARG footprint, both methods resulted in emissivities with a difference  
190 of 0.01 RMS. The average of these area average emissivities, between 2006/01/01 and  
191 2006/11/30, gave an overall estimate of  $0.93 \pm 0.01$ . Since no diurnal variation is as-  
192 sumed, the emissivity value,  $\epsilon$ , was fixed to this value.

193 The LST retrievals from MOD/MYD11A2 are (essentially) 8-day averages from two  
194 retrievals per calendar day, to compromise between data availability and time resolution.  
195 Since the time resolution is insufficient for per profile LST specification, the retrievals are  
196 instead used to estimate the ratio between the LST of the MODIS footprint ( $\sim 500$  m  
197 about the AMF) and that of the ARG footprint. This ratio is then used to scale the  
198 AMF LST, to remove the potential surface systematic bias. By using a scaling, the only  
199 assumption made is that the MODIS footprint LST about the AMF has a constant scaling  
200 relationship with the AMF LST. The MODIS resolution is sufficiently small to negate  
201 effects of the river or its adjacent paddy fields ( $\geq 3.5$  km SW of the airport location).  
202 High resolution imagery and local cartography also suggest that there are no obvious  
203 changes in land cover which could invalidate the assumption. The MODIS-based scaling  
204 was calculated over all 8-day periods in the year: the ARG footprint LST estimate,  $T_{ARG}$ ,  
205 from the AMF LST value,  $T_{AMF}$ , was found to best obey a linear transform,

$$T_{ARG} = T_{AMF} \times (0.93 \pm 0.02) + (18.5 \pm 5.8).$$

206 The AMF LST used here,  $T_{AMF}(t)$ , is not directly measured but is derived by fitting the  
 207 derived temperature (from the upwelling pyrgeometer),  $T_{deriv}(t)$ , to a retrieved temper-  
 208 ature (from the upwelling IR thermometer),  $T_{IRT}(t)$ . This procedure begins by deriving  
 209 temperatures from upwelling fluxes,  $F_{ULR;AMF}(t)$ , assuming black body & Lambertian  
 210 emission,

$$T_{deriv}(t) = \left( \frac{F_{ULR;AMF}(t)}{\epsilon\sigma} \right)^{\frac{1}{4}}.$$

211 The diurnal-mean of  $T_{deriv}$  is then scaled to equal that of  $T_{IRT}$ , and this scaling is  
 212 applied to form the LST time series,  $T_{AMF}(t)$ ,

$$T_{AMF}(t) = T_{deriv}(t) \frac{\overline{T}_{deriv}}{\overline{T}_{IRT}}. \quad (1)$$

213 This derivation of  $T_{AMF}$  was implemented because a significant difference is observed  
 214 in the diurnal variation between the pyrgeometer and IR thermometer, especially at local  
 215 noon. Since the interest here is in modelling diurnal radiation variations, it was thought  
 216 more prudent to use the pyrgeometer to return the diurnal variations and to use the  
 217 thermometer for the absolute values.

### 3. SURFACE RESULTS

218 The results of the ES96 calculations are compared to the measurements from the AMF  
 219 in this section. These initial simulations assume pristine sky conditions (cloud- & aerosol-  
 220 free), and demonstrate how omitting aerosol affects the surface LW radiation calculations.

221 The calculated aerosol direct effect at the surface is then analysed in conjunction with  
222 retrievals of aerosol optical depth to demonstrate that this effect does account for the  
223 majority of the difference between calculations and observations.

224 The time series of measurements and simulations are shown in figures 1, 2, & 3 for the  
225 three flux components: surface downwelling, surface upwelling, and OLR. The observed  
226 less calculated (obs-calc) flux differences are shown in figures 4, 5, & 6. A comparison of  
227 the modelled pristine surface downwelling fluxes with independent calculations (*Mlawer,*  
228 *personal communication*), using the LBLRTM code, shows a correlation  $r$  value of 0.95.  
229 Therefore the ES96 results are in excellent correspondence with the more precise LBLRTM  
230 results.

### 3.1. Upwelling surface radiation

231 The obs-calc comparison shows a noticeable difference for the upwelling surface flux  
232 (ULR) but this is expected since different surface properties are deliberately used in the  
233 simulations compared to those measured at the AMF. Using figures 2 & 5, from January  
234 to September the ULR obs-calc difference increases with increases in measured ULR. From  
235 September onwards, however, the obs-calc difference *decreases* with increases in measured  
236 ULR. The reason for this change in correlation between the difference and the observed  
237 flux is not clear; however the obs-calc difference range over the year is  $\pm 10 \text{ Wm}^{-2}$  which  
238 is only of the order 5% of the absolute value of the ULR. (In a companion paper [*Settle*  
239 *et al.*, 2008], using a different satellite LST retrieval dataset, it is found that the AMF  
240 ULR measurements are, over 2006 as a whole,  $\sim 4 \pm 4 \text{ Wm}^{-2}$  greater than the ARG area  
241 estimate which is consistent with this analysis.)

### 3.2. Downwelling surface radiation

242 The observed surface downwelling fluxes (DLR) show the effects of changes in CWV  
243 and temperature, figure 1. In time, the wet season onset and retreat (circa days 120  
244 and 300) is the largest driver of DLR whilst temperature fluctuations are most evident  
245 in the dry season [*Slingo et al.*, 2008b]. The calculations model the overall flux trends,  
246 and do so more accurately in terms of diurnal variability than a simple parameterisation  
247 [*Prata*, 1996]. Nonetheless, a significant obs-calc under-estimate exists, especially in the  
248 dry season.

249 The scatter of the obs-calc differences with CWV, figure 7 (upper panel), demonstrates  
250 a clear link between flux residuals and the atmospheric profile. If there were a bias in  
251 either temperature or water vapor, then the lower limit of the obs-calc difference would  
252 not be expected to be close to zero regardless of CWV value. In particular, only a few  
253 points show a negative obs-calc value (1 % are more than the measurement error below  
254 zero) whilst a large number (40 %) have a difference of  $\leq 10 \text{ Wm}^{-2}$  (twice the measurement  
255 error). In contrast, the upper limit of the flux differences decreases with an increase of  
256 CWV. These observations are consistent with the aerosol direct effect being primarily  
257 responsible for the difference: as the CWV lessens, the (8 – 13  $\mu\text{m}$ ) IR window becomes  
258 optically thinner which allows the direct effect to become relatively larger. This is most  
259 evident during the dust storm of March 2006 [*Slingo et al.*, 2006] when CWV was  $\sim 1 \text{ cm}$ .  
260 During this event the optical depth reached 3.4, and the highlighted points in figure 7  
261 show the particularly large obs-calc values,  $\sim 100 \text{ Wm}^{-2}$  coincident with the passing of  
262 the storm front over Niamey.

263 The obs-calc analysis was repeated with zenith radiances from the AERI. Since the  
264 intention here is to establish the accuracy of the temperature and humidity profiles, it is  
265 useful to compare radiances in several regions of the spectrum where temperature, water  
266 vapor, and aerosol in turn have a dominating effect. The band-passes utilised and their  
267 primary sources of emission are shown in table 3. Band #4 is dominated by CO<sub>2</sub> emission  
268 and, since the vertical distribution and quantity are well established *a priori*, it becomes  
269 a test of temperature. Similarly, band #8 is dominated by water vapor and temperature,  
270 so can be used to verify the boundary layer water vapor quantity. Finally, band #5 has  
271 the same contributions but at far lower optical depths, and is where the effect of aerosol  
272 emission would be most notable. Figure 9 shows scatter plots for these three bands. The  
273 dashed lines mark the expected 1:1 relationships, which are obeyed to within 1 % for bands  
274 #4 and #8. For band #5, there is a consistent under-estimate by the calculations, and is  
275 reminiscent of figure 7. Note also that there is virtually no predicted excess radiation. As  
276 these narrowband radiance comparisons are consistent with the comparisons of broadband  
277 fluxes, it shall be assumed that any bias in pyrgeometer fluxes is within its measurement  
278 error.

279 To quantify the direct effect, a correlation between the diurnal-average of obs-calc flux  
280 difference and coarse-mode AOT can be made. (The diurnal-average can only be calcu-  
281 lated for those days with four sonde launches at cloud-free times.) The following assump-  
282 tions are made: AOT at the AERONET site (Banizoumbou) is correlated with that at  
283 the AMF (Niamey), the longwave dust emission is a (simple) function of the shortwave  
284 AOT, and that changes in vertical structure of aerosol within the atmosphere are neg-  
285 ligible. Comparing 561 near-contemporaneous AERONET retrievals from the two sites: the

286  $r$  correlation coefficient is 0.91. The second assumption is validated by the companion  
 287 paper [Turner, 2008], and it is noted that the 1020 nm AOT varies between 0.03 and  
 288 4.07 during the year. The final assumption rests on temperature variations. By taking  
 289 diurnally-averaged values, the change in emission due to per-day temperature variability is  
 290 reduced. Furthermore, the diurnal-mean temperature, averaged between the surface and  
 291 800 hPa, is  $298 \pm 3$  K. A simple model for vertical distribution of aerosol is an even quantity  
 292 (density) with altitude from the surface to 800 hPa. The mean temperature averaged over  
 293 this altitude, and then raised to the 4th power, becomes an aerosol emission-equivalent  
 294 value (assuming a black body approximation). The standard deviation from the mean of  
 295 this emission-equivalent value during 2006 is 4%. Hence, the direct effect variation can  
 296 be expected primarily from changes in (vertically) integrated aerosol concentration.

297 The flux residual-AOT correlation is shown in figure 8. Given the direct effect efficacy  
 298 is controlled by the opacity of the IR window, a set of simple fits were made to understand  
 299 the dependence. The data are binned into CWV intervals of 0–1 cm, 1–1.5 cm, 1.5–2.5 cm,  
 300 & 2.5 cm and greater. The form of fit used is,

$$\bar{\Delta}(F_{DLR}) \equiv \overline{F_{DLR;observed} - F_{DLR;calculated}} = \alpha + (\beta \bar{\tau}) / (1 + \bar{\tau}), \quad (2)$$

301 where the averages represent appropriate diurnal means. This equation was chosen  
 302 empirically to obey the principle that emission must asymptote at high values of AOT  
 303 but be linear for low values. The fit values of  $\alpha$  and  $\beta$ , representing the obs-calc flux  
 304 difference for no aerosol (RT profile error) and the forcing per unit scaled optical depth  
 305 (measure of the direct effect) are shown in table 4. The results show that the forcing per  
 306 unit scaled optical depth,  $\beta$ , decreases as the CWV increases as expected.

307 These fits can be used to ‘correct’ the diurnal mean pristine ES96 fluxes for the aerosol  
308 direct effect, and these corrected fluxes are used to repeat the obs-calc analysis. Figure  
309 7 (bottom panel) shows the scatter of these residuals with CWV, and it can be seen  
310 that the median for all bins is, as expected, near zero ( $\leq 1.5 \text{ Wm}^{-2}$ ) and each has a  
311 similar variance. This latter result simply confirms the result from the fit parameters: the  
312 uncertainty in the fits remains relatively constant, regardless of CWV.

313 As CWV increases, the offset for zero optical depth,  $\alpha$ , also increases although when  
314 CWV is less than 1 cm, the value is consistent with zero. The cause for the increase  
315 could be a result of the fitted function being inadequate due to non-linearities in water  
316 vapor emission. Alternately, it was noted that the ratio of AERONET-derived CWV with  
317 that from the AMF microwave radiometer is  $0.83 \pm 0.08$ , which could implicate the AOT  
318 retrievals.

319 These results are all consistent with the modelled, pristine fluxes being an unbiased  
320 representation of the emission due to the atmospheric gases and water vapor alone. The  
321 obs-calc difference then represents the aerosol direct effect to within errors that are rea-  
322 sonable, given visible/near-IR retrievals are proxies for LW optical depths. This statement  
323 is less certain for the wet season, where CWV is larger than 2.5 cm.

#### 4. TOP OF ATMOSPHERE RESULTS

324 Having compared the ES96 calculations at the surface with observations, the equivalent  
325 analysis with TOA observations is presented here. The comparison of pristine radiation  
326 calculations at TOA is less straightforward due to disagreements in radiance-to-flux con-  
327 version from ES96 and the GERB Edition 1 processing. This necessitates including a  
328 simplified aerosol representation into the RT profiles, using the previously calculated di-

329 rect effect at the surface. The resulting clear sky (cloud-free with aerosol) calculations  
330 then allow comparisons with TOA measurements using *a priori* profiles.

331 The top of atmosphere upwelling flux (OLR) is dependent on the emissivity & temper-  
332 ature of the atmosphere as well as the surface upwelling flux. From the surface analysis in  
333 the previous section, the atmospheric components (less aerosol) are found to be consistent  
334 with observed values to within the measurement errors. The surface upwelling flux com-  
335 parison showed that the estimate of the GERB ARG footprint flux is, however, biased  
336 with respect to the AMF measurements. Thus one benefit of analysing the OLR is in  
337 indirectly evaluating this surface flux. Since the quantity measured by GERB at TOA is  
338 radiance, the OLR is actually a derived quantity [Dewitte *et al.*, 2008] which necessarily  
339 contains assumptions about the atmospheric profile under each pixel and the associated  
340 surface properties. For the Edition 1 fluxes, a known issue is the omission of aerosol from  
341 the radiance-to-flux conversion. As the surface results show, there are instances of large  
342 aerosol direct effects. Hence evaluating the radiance-to-flux conversion is a prerequisite  
343 before being able to accurately compare the ES96 and GERB ARG OLR fluxes.

344 Initially, the GERB SHI and ARG product fluxes are compared over Niamey. The  
345 significant difference between these is the surface footprint of each product: the SHI pixel  
346 area is  $\sim 9 \times 9$  km vs. the ARG pixel  $\sim 45 \times 45$  km. For the relevant pixels covering  
347 Niamey, this is particularly important since the River Niger affects respectively  $\sim 10\%$   
348 and  $\sim 40\%$  of the ARG and SHI pixel areas. From coincident cloud-free times during 2006,  
349 the ratio of fluxes between the ARG and SHI products is  $0.99 \pm 0.06$ . (For comparison,  
350 the ARG flux varies by more than 1% only when the distance, between the centre of  
351 the pixel covering Niamey and the comparison pixel, exceeds 100 km.) Together with the

352 prior assumption of a laterally homogenous atmosphere, the implication is that surface  
353 property ratios will have the same values: the ARG-area to SHI-area ratio for surface  
354 temperatures is  $0.997 \pm 0.001$ , and the same for emissivities is  $0.98 \pm 0.01$ . The good  
355 agreement between the two TOA fluxes and the similar agreement in surface property  
356 retrievals implies that these retrievals are sufficiently accurate for this work.

#### 4.1. Pristine sky calculations

357 As the surface emissivities are fixed (0.93) in the profiles, the use of scaling the LST  
358 will first be investigated. The profiles are aerosol-free so a non-zero obs-calc difference is  
359 expected; it is the difference between using scaled, pyrgeometer-derived and unscaled, IR  
360 thermometer-measured temperature that is of interest. The obs-calc differences between  
361 GERB ARG and ES96 radiances are displayed in table 5. The change in the obs-calc  
362 difference when the scaled LST is used, for all time bins, is within the stated interquartile  
363 range. The percentages show the change is consistent in that day-times (11 & 17 UT)  
364 show a decrease in the obs-calc difference whereas night-times show an increase. This  
365 shows that the diurnal variation of the calculated radiances is reduced by using the scaled  
366 LST, which will now be considered valid.

367 The next analysis is an analogous comparison between the GERB ARG radiance and  
368 GERB ARG flux obs-calc differences. These differences are displayed in table 6, and  
369 also subdivided into the two seasons. The most clear trend is that the obs-calc radiance  
370 values show larger, relative differences during the diurnal cycles than the equivalent flux  
371 differences. If the radiance-to-flux conversion used in GERB Edition 1 processing and  
372 that in the ES96 code were equivalent then this would not be expected: there would be a

constant scaling factor when comparing radiance and flux obs-calc values. This argument  
 can be substantiated by plotting the angular conversion factor,  $R$ ,

$$R(\theta, \phi; \Omega) = \frac{\pi L_{OLR}(\theta, \phi)}{F_{OLR}(\theta, \phi)}, \quad (3)$$

where  $(\theta, \phi)$  are the viewing angles between the satellite and the atmosphere,  $\Omega$  represents the state vector of the atmosphere and surface,  $L_{OLR}$  is the measured TOA radiance and  $F_{OLR}$  is the retrieved flux. Here, because GERB and the AMF are fixed relative to each other, the angular coordinates remain constant and the changes are in  $\Omega$ . Figure 11 (upper panel) shows  $R$  from ES96 calculations and GERB ARG plotted against the profile surface temperature. (Surface temperature is a value in  $\Omega$  and also a proxy for time since the coldest temperatures correspond to pre-dawn and the hottest to near-noon, 06 UT & 11 UT approximately.) It is clear that the derived values of  $R$  follow a substantially linear relationship with surface temperature. Using a linear model to fit the two collections of  $R$ , results in the following,

$$\begin{aligned} \bar{R}_{GERB}(T_{surface}) &= 0.85 + 6.74 \times 10^{-4} T_{surface}, \\ \bar{R}_{pristine;ES6}(T_{surface}) &= 0.55 + 1.66 \times 10^{-3} T_{surface}. \end{aligned} \quad (4)$$

Notably, the gradients vary by more than a factor of 2. The consequence is that, for equal radiances, the ES96 fluxes would change more slowly than GERB fluxes between the 06 UT and 11 UT time bins. The impact on the flux obs-calc differences would be a smaller relative difference between these two time bins than expected from the equivalent radiance obs-calc differences, which is the result seen.

## 4.2. Clear sky calculations

390 The discrepancy between the GERB- and ES96-derived angular conversion factor im-  
 391 plies that even if radiance-closure were achieved (consistent radiances between measure-  
 392 ments and model), then fluxes will have a time varying non-zero obs-calc difference. How-  
 393 ever, the previous section assumed no aerosol was present. To understand the magnitude  
 394 of discrepancy between the cloud-free GERB ARG fluxes and ES96 fluxes, it is necessary  
 395 to repeat the previous work with aerosol included in the simulations. The addition of  
 396 aerosol into the RT profiles is via the calculated aerosol direct effect, using the results in  
 397 section 3.2. Because the comparisons will only be made with TOA measurements, this  
 398 ensures suitable independence of the calculations.

399 The clear sky profiles use the pristine sky profiles, with an added aerosol dust layer. The  
 400 aerosol profile is specified as mass mixing ratios, estimated as follows. First, an empirical  
 401 profile is created,

$$\text{MMR}_{\text{dust;template}} = \overline{\text{MMR}} \exp \left[ -\frac{(p - p_m)^2}{2\sigma^2} \right], \quad (5)$$

402 where  $p$  is profile level pressure,  $\overline{\text{MMR}}$  is a physically realistic constant,  $p_m = 933$  hPa  
 403 and  $\sigma = 210$  hPa. The parameter values were chosen to produce a plausible profile  
 404 [Johnson *et al.*, 2008] which places 99% of the aerosol below 7.3 km and 50% below 1.7 km.  
 405 Next, the dust profile is scaled equally at each level such that the resulting calculations of  
 406 DLR are equal to AMF measurements i.e. the derived aerosol direct effect is accounted  
 407 for. To do this, an estimate of the scaling,  $c$ , is calculated. Initially, the effect of scaling  
 408 is established by fitting the parameters  $A$  and  $B$  in the following function,

$$F_{DLR;c} = F_{DLR;c=0} + A(1 - e^{-B \times c}), \quad (6)$$

409 for several values of  $c$  ranging from 0 to 40. (The upper limit corresponding to a dust  
 410 column mass of  $25.6 \text{ gm}^{-2}$ .) The term  $F_{DLR}$  is the DLR, whilst  $c$  is the profile scaling  
 411 factor. (Hence,  $F_{DLR;c=0}$  is the pristine value viz section 3.2.) Having obtained  $A$  and  $B$   
 412 for each profile, equation 6 can be inverted to obtain an estimate of  $c$  for a measurement  
 413 of  $F_{DLR;AMF}$ ,

$$c_{estimate} = -\ln \left[ 1 - \frac{F_{DLR;AMF} - F_{DLR;c=0}}{A} \right] / B. \quad (7)$$

414 The scaled dust profile is then,

$$\text{MMR}_{dust;estimate} = c_{estimate} \times \text{MMR}_{dust;template}. \quad (8)$$

415 An advantage of using equation 7, rather than the fits to AERONET data, is that  
 416 diurnal variations [*N'tchayi Mbourou et al., 1997*] are more accurately estimated. The error  
 417 estimates for  $c_{estimate}$  occur from the variances of  $F_{DLR;AMF}$ , and these are propagated to  
 418 the TOA radiation results: 50% & 84% of profiles have TOA radiance standard deviations  
 419 of less than 5% & 20%.

420 Once again, a comparison can be made with the surface radiances. With the pristine  
 421 simulations, a significant deficit was found in the band #5 comparison (figure 9). In-  
 422 cluding the aerosol derived from the broadband flux measurements, figure 10 shows a  
 423 significantly better adherence to the 1:1 relationship in the scatter plot. Hence, since  
 424 the RT calculations are consistent with AERI narrowband radiances all three bands, the

425 aerosol profiles are considered consistent for surface simulations and now used for TOA  
 426 simulations.

427 The clear sky obs-calc differences for GERB ARG radiances and fluxes are shown in  
 428 table 7. They are also shown as a box-whisker plot, with the equivalent results from  
 429 pristine comparisons, in figure 12. The notable change when aerosol is included is that  
 430 the radiance differences become more equal across times, with near equivalence in the dry  
 431 season and some remnant variation in the wet season. As percentages, the aerosol-included  
 432 differences are  $-2\%$  (dry) to  $-5\%$  (wet) of the GERB ARG radiance. Comparisons of  
 433 GERB and CERES LW radiances (*Dewitte et al. [2008] & Clerbaux, in preparation*) show  
 434 that under equivalent clear-sky conditions as used in this work, and within the whole  
 435 GERB field-of-view, the ratio between the GERB/CERES satellite radiance measurement  
 436 is  $\sim 98\%$ . Hence, in the dry seasons, the calculated radiance at any time is consistent  
 437 with the observations to within their uncertainty.

438 The fluxes, as expected, behave differently from the radiances. The clear sky fluxes  
 439 show an opposite trend with time bin when compared with the pristine fluxes: the obs-  
 440 calc difference becomes smaller in the day time, rather than larger. Figure 11 (bottom  
 441 panel) shows how the angular conversion factor,  $R$ , is changed by including aerosol. The  
 442 fit to the clear sky ES96  $R$  values, c.f. equations 4, is,

$$\overline{R}_{clear;ES96}(T_{surface}) = 0.41 + 2.15 \times 10^{-3} T_{surface}. \quad (9)$$

443 The gradient of the fit to  $R$  is therefore increased by the presence of aerosol:  $\overline{R}_{clear;ES96}$   
 444 now increases more than three times as rapidly with surface temperature than  $\overline{R}_{GERB}$ .  
 445 Consequently, the discrepancies in flux obs-calc are largest for the hottest surfaces, which

446 corresponds here to 11 UT. In order to improve the divergence calculations in the fol-  
 447 lowing section, it is possible to create a new estimate of TOA OLR. This product,  
 448  $F_{OLR;ARG;R=ES96}$ , which shall be called the GERB/ES96 hybrid, uses the angular con-  
 449 version factor from each ES96 calculation,  $R_{clear;ES96}(t)$ , to create a flux from the contem-  
 450 pous GERB ARG radiance,  $L_{OLR;ARG}(t)$ ,

$$F_{OLR;ARG;R=ES96}(t) = \frac{\pi \times L_{OLR;ARG}(t)}{R_{clear;ES96}(t)}, \quad (10)$$

451 where  $t$  are the cloud-free times. Figure 13 plots the time series (upper panel) of the  
 452 GERB ARG Edition 1 OLR,  $F_{OLR;ARG}$ , with the hybrid OLR,  $F_{OLR;ARG;R=ES96}$ , and  
 453 their difference (lower panel). At night, the difference is small and generally the hybrid  
 454 OLR is marginally larger ( $0.5_{-1.2}^{+0.8} \text{ Wm}^{-2}$ ) than the Edition 1 OLR. During the day the  
 455 hybrid OLR is smaller ( $6.1_{-1.6}^{+2.5} \text{ Wm}^{-2}$ ), especially in the dry season when aerosol loading is  
 456 high. In particular, during the March dust storm on 2006/03/07 11 UT, the hybrid OLR  
 457 is  $\sim 12 \text{ Wm}^{-2}$  lower, and on 2006/04/03 11 UT, the hybrid OLR shows the maximum  
 458 difference in this time series of  $\sim 15 \text{ Wm}^{-2}$ . For this latter date, the difference is a  
 459 consequence of three factors: near annual-maximum surface temperature, near annual-  
 460 minimum column water vapor, and above-average dust loading ( $\text{AOT}(1020 \text{ nm})=0.85$  c.f.  
 461 the 2006-average of 0.6).

462 In the context of the clear sky OLR fluxes, the hybrid OLR suggests that only the  
 463 06 UT and 23 UT obs-calc flux difference comparisons in table 7 are accurate and that the  
 464 daytime differences are biased by the value of the inter-quartile range.

## 5. LONGWAVE ATMOSPHERIC DIVERGENCES

465 The previous two sections have analysed the surface and TOA radiation to derive a best  
466 estimate of the longwave fluxes. These fluxes are: the surface upwelling flux, which is from  
467 simulations using a GERB ARG-area scaled temperature, the surface downwelling flux,  
468 which is also from the simulations (but with aerosol, so equivalent to AMF measurements),  
469 and the TOA upwelling flux, which is from the GERB/ES96 hybrid OLR. A summary of  
470 these is shown in table 8.

471 A companion paper [*Slingo et al.*, 2008b] analyses the diurnally averaged divergence  
472 by using only the measured values ( $F_{DLR;AMF}$  &  $F_{ULR;AMF}$  from the AMF and  $F_{OLR;ARG}$   
473 from GERB Edition 1). The results in this work permit a similar calculation for cloud-free  
474 times, using any one of three ‘flux component collections’, which are defined as follows:

- 475 1. the best estimates (as described above),
- 476 2. or simulation only,
- 477 3. or observations only.

478 Figure 14 shows three divergence estimates for 2006, and the numerical values are in  
479 table 9. The diurnal trend is similar between each calculation, and the inter-quartile ranges  
480 do not typically exceed the difference between bin medians. These results correspond to  
481 a key result in the companion paper [*Slingo et al.*, 2008b]: the diurnal mean divergence  
482 for cloud-free times is  $-167_{-9}^{+7} \text{ Wm}^{-2}$  during 2006. In other words, the average divergence  
483 is relatively constant through the year, regardless of season. In contrast, the diurnal  
484 amplitude of divergence has a larger change.

485 In comparing the three divergence results with each other, the simulation divergences  
486 show the most cooling for each bin whereas the observation divergences show the least.  
487 Additionally, over the diurnal cycle, the amplitude of the former is larger than the lat-

488 ter. Comparing the best estimate divergences with those from observations, the latter  
489 shows more cooling at 11 UT, a similar amount at 17 UT and less at 06 UT and 23 UT.  
490 The amplitude of the diurnal cycle of the former is larger than the latter. As percent-  
491 ages, however, the differences between the medians of best estimate divergences from the  
492 observation equivalents are  $\sim -1$  to  $-3\%$ .

493 The expected diurnal mean difference would then be typically  $\sim 1\%$ , or  $\sim 2 \text{ Wm}^{-2}$ . In  
494 the context of GERB ARG and AMF flux measurement errors, this difference is small.  
495 It does also validate the approach in the companion paper [*Slingo et al.*, 2008b] of using  
496 observation-only flux components to study the resulting variability in divergence with  
497 other variables such as AOT and CWV. However, to study more finely time resolved  
498 divergences, such as the 4 time bins here, the nature of flux components used can result  
499 in a bias which *is* larger than the measurement errors.

## 6. CONCLUSION

500 In this work, a comparison has been made between the observed radiative fluxes and  
501 radiances in the thermal region of the spectrum, at both the surface and top of atmosphere.  
502 Utilising the high time resolution of measurements from both locations, aerosol- and cloud-  
503 free contemporaneous calculations were made for four sonde launch times per day, for 361 days  
504 of 2006. At the surface, flux comparisons were made of the upwelling and downwelling  
505 components. The upwelling flux was found to differ substantially, and regularly, from the  
506 observed measurements but this is accounted for by the attempt made to model flux from  
507 the wider area to be consistent with the satellite footprint.

508 The simulated, aerosol-free downwelling flux was found to behave principally as the  
509 observed values, with the changes in column water vapor and temperature. The residual

510 differences were found to be strongly correlated with column water vapor and consistent  
511 with the aerosol direct effect. This was verified by comparison of radiances from zenith-  
512 pointing observations in three wavebands, which separately verified the temperature and  
513 humidity profiles in the lower troposphere. A correlation of the flux residuals with visible  
514 AERONET optical depth retrievals allowed for a simple estimate of the direct effect.

515 A similar analysis was carried out between the top of atmosphere observations of ra-  
516 diances and fluxes and the simulated values. Since the observed fluxes are a product, a  
517 comparison of radiances was initially undertaken to establish the effect of the surface tem-  
518 perature scaling and surface emissivity derivations. These showed an improvement when  
519 compared to using the observed surface temperature from the AMF. The comparison be-  
520 tween simulated and observed radiances and the same for fluxes made evident a disparity  
521 that was attributed to the radiance-to-flux conversion process. To more fully understand  
522 this disparity, the simulations then moved to using a inferred aerosol representation.

523 Utilising the measured direct effect from the surface broadband fluxes, to specify the  
524 aerosol loadings and a simplified vertical structure, comparisons were made at the surface  
525 with measured radiances. This verified that the overall direct effect at the surface was well  
526 characterized. Using these profiles, the top of atmosphere radiance and flux comparison  
527 was repeated. It was found that during the dry season, where column water vapor is be-  
528 low  $\sim 2.5$  cm, the simulated radiances showed negligible variation relative to the observed  
529 values and were consistent with GERB-CERES comparisons. Therefore, within the ob-  
530 served errors, radiance closure was achieved in the dry season at both the surface and  
531 top of atmosphere when clouds are not present. Some residual diurnal variation between  
532 radiances remained in the wet season.

533 The top of atmosphere flux comparison showed significant differences, unlike the radi-  
534 ance comparison, in both dry and wet season. Again, this was consistent with a difference  
535 in the radiance-to-flux conversion between the product algorithm and the radiative trans-  
536 fer code used here. (A known omission in the GERB Edition 1 product algorithm is the  
537 absence of aerosol effects.) Given the agreement of simulated and observed radiances,  
538 but not for the fluxes, a hybrid OLR product was created: using the simulated (ES96)  
539 radiance-to-flux conversion and the observed (GERB) radiances.

540 Using the cloud-free, aerosol-present simulations, it became possible to calculate the  
541 atmospheric heating (divergence) using one of three flux collections: using observations  
542 from the AMF and GERB Edition 1 ARG only, using the ES96 simulated fluxes only,  
543 or using a combination of model and measurements. The latter is described as the ‘best  
544 estimate collection’. The three estimates, treated as averages for the 4 time bins through-  
545 out 2006, were found to show both similar diurnal variations across the bins and similar  
546 inter-quartile ranges within each bin. However, a comparison of the values per bin from  
547 the three estimates showed differences as large as 5 %. Therefore for time resolved calcula-  
548 tions, care must be taken in using consistent calculations, which here only truly applies to  
549 the simulated flux collection. This collection may remain biased, especially in the wet sea-  
550 son, but has a good correspondence as regards the diurnal variation with the divergences  
551 from the best estimate collection.

552 Future work using the RADAGAST dataset can utilize the infra-red retrievals of mineral  
553 dust [*Turner*, 2008], and associated retrievals of chemical speciation, to better characterise  
554 the aerosol environment. This will then allow a more detailed investigation into the  
555 apparent difference between radiances at the top of atmosphere in the wet season, which

556 may be an indicator of incorrect humidity specification. Improving the top of atmosphere  
557 flux retrievals in the presence of aerosol, which is shown to be omnipresent in Niamey  
558 during 2006, is another area which merits study especially given the prominent view of  
559 the Sahara that the GERB instruments have. Establishing if the results presented here  
560 are consistent for instrument view angles and for different dust sources will be important  
561 in this task. Finally, the omission of clouds results in this work completing only one part  
562 of the task in RADAGAST and several opportunities subsequently present themselves,  
563 such as using the clear sky simulations to model the cloud forcing using the data or using  
564 cloud retrievals to directly model cloud effects within the radiative transfer code.

### 565 **Acknowledgments.**

566 NAB thanks Helen Brindley for fruitful discussion on GERB radiance-to-flux issues. NAB  
567 is funded by NERC grant NE/D002370/1. The GERB Edition 1 data were obtained from the  
568 GGSPS, Rutherford Appleton Laboratory, <http://ggsp.s.rl.ac.uk/>. The IR emissivity data  
569 were obtained from CIMMS, University of Wisconsin-Madison, <http://cimss.ssec.wisc.edu/irem/s/>. The MODIS data are distributed by the Land Processes Distributed Active Archive  
570 Center (LP DAAC), located at the U.S. Geological Survey (USGS) Earth Resources Observation  
571 and Science Center (EROS), <http://LPDAAC.usgs.gov/>. The AMF data were obtained from  
572 the ARM archive, <http://www.archive.arm.gov/>, provided by the U.S. Department of Energy  
573 as part of the Atmospheric Radiation Measurement Program Climate Research Facility. The  
574 NWCSAF cloud mask was obtained via the EUMETSAT on-line archive, <http://archive.eumetsat.org/>. The AERONET data were obtained from, <http://aeronet.gsfc.nasa.gov/>,  
575 with thanks to Didier Tanré (LOA, Université des Sciences et Technologies de Lille) & Rick

578 Wagener (Brookhaven National Laboratory, NY) for their effort in establishing and maintaining  
579 the sites at Banizoumbou and Niamey.

## References

- 580 Barkstrom, B. R. (1984), The Earth Radiation Budget Experiment (ERBE), *Bull. Am. Meteorol.*  
581 *Soc.*, , 65, 1170–1185.
- 582 Claquin, T., M. Schulz, Y. Balkanski, and O. Boucher (1998), Uncertainties in assessing radiative  
583 forcing by mineral dust, *Tellus*, 50, 491-, doi:10.1034/j.1600-0889.1998.t01-2-00007.x.
- 584 Clerbaux, N., S. Dewitte, L. Gonzalez, C. Bertrand, N. B., and A. Ipe (2003), Outgoing longwave  
585 flux estimation: improvement of angular modelling using spectral information, *Rem. Sens.*  
586 *Env.*, 85, 389–395.
- 587 d’Almeida, G. A., P. Koepke, and E. P. Shettle (1991), ”*Atmospheric Aerosols. Global Climatology*  
588 *and Radiation Characteristics.*”, A. Deepak Publishing, Hampton VA, USA.
- 589 Derrien, M., and H. Le Gleau (2005), MSG/SEVIRI cloud mask and type from SAFNWC, *Int.*  
590 *J. Remote Sensing*, 26, 4707–4732, doi:10.1080/01431160500166128.
- 591 Dewitte, S., L. Gonzalez, N. Clerbaux, A. Ipe, C. Bertrand, and B. De Paepe (2008), The  
592 Geostationary Earth Radiation Budget Edition 1 data processing algorithms, *Advances in*  
593 *Space Research*, 41, 1906–1913, doi:10.1016/j.asr.2007.07.042.
- 594 Dey, S., and S. N. Tripathi (2008), Aerosol direct radiative effects over Kanpur in the Indo-  
595 Gangetic basin, northern India: Long-term (2001-2005) observations and implications to re-  
596 gional climate, *J. Geophys. Res.*, , 113, 4212-, doi:10.1029/2007JD009029.
- 597 Edwards, J. M., and A. Slingo (1996), Studies with a flexible new radiation code. I: Choosing  
598 a configuration for a large-scale model, *Q. J. R. Meteorol. Soc.*, , 122, 689–719, doi:10.1256/

599 smsqj.53106.

600 Ellingson, R. G., J. Ellis, and S. Fels (1991), The intercomparison of radiation codes used in  
601 climate models: Long wave results, *J. Geophys. Res.*, , *96*, 8929–8953.

602 Harries, J. E., et al. (2005), The Geostationary Earth Radiation Budget Project, *Bull. Am.*  
603 *Meteorol. Soc.*, , *86*, 945–960.

604 Hartmann, D. L. (1994), *Global Physical Climatology*, 411 pp., Academic Press, New York.

605 Henderson, P. W. (2006), Evaluations of the Met Office forecast model using observations from  
606 the Atmospheric Radiation Measurement program, Ph.D. thesis, University of Reading.

607 Holben, B. N., et al. (2001), An emerging ground-based aerosol climatology: Aerosol optical  
608 depth from AERONET, *J. Geophys. Res.*, , *106*, 12,067–12,098, doi:10.1029/2001JD900014.

609 Hucek, R., L. Stowe, and R. Joyce (1996), Evaluating the Design of an Earth Radiation Budget  
610 Instrument with System Simulations. Part III: CERES-I Diurnal Sampling Error, *J. Atmos.*  
611 *Ocean. Technol.*, *13*, 383-, doi:10.1175/1520-0426(1996)013.

612 Jacobowitz, H., H. V. Soule, H. L. Kyle, and F. B. House (1984), The Earth Radiation Budget  
613 (ERB) experiment - An overview, *J. Geophys. Res.*, , *89*, 5021–5038.

614 Johnson, B. T., B. Heese, S. A. McFarlane, P. Chazette, A. Jones, and N. Bellouin (2008),  
615 Vertical distribution and radiative effects of mineral dust and biomass burning aerosol over  
616 West Africa during DABEX, *J. Geophys. Res.*, , *Accepted*, Y, doi:10/Z.

617 Knuteson, R. O., et al. (2004), Atmospheric Emitted Radiance Interferometer. Part I: Instrument  
618 Design, *Journal of Atmospheric and Oceanic Technology*, *21*, 1763-, doi:10.1175/JTECH-1662.  
619 1.

620 Long, C. N., and T. P. Ackerman (2000), Identification of clear skies from broadband pyranometer  
621 measurements and calculation of downwelling shortwave cloud effects, *J. Geophys. Res.*, , *105*,

622 15,609–15,626, doi:10.1029/2000JD900077.

623 Martin, G. M., M. A. Ringer, V. D. Pope, A. Jones, C. Dearden, and T. J. Hinton (2006),  
624 The Physical Properties of the Atmosphere in the New Hadley Centre Global Environmental  
625 Model (HadGEM1). Part I: Model Description and Global Climatology, *J. Clim.*, *19*, 1274,  
626 doi:10.1175/JCLI3636.1.

627 Miller, M., and A. Slingo (2007), The Arm Mobile Facility and Its First International Deployment:  
628 Measuring Radiative Flux Divergence in West Africa, *Bull. Am. Meteorol. Soc.*, , *88*, 12291244,  
629 doi:10.1175/BAMS-88-8-1229.

630 Miller, R. L., I. Tegen, and J. Perlwitz (2004), Surface radiative forcing by soil dust aerosols and  
631 the hydrologic cycle, *J. Geophys. Res.*, , *109*, 4203-, doi:10.1029/2003JD004085.

632 N'tchayi Mbourou, G., J. J. Bertrand, and S. E. Nicholson (1997), The Diurnal and Seasonal  
633 Cycles of Wind-Borne Dust over Africa North of the Equator, *J. Appl. Meteorol.*, *36*, 868–882.

634 Ohmura, A., et al. (1998), Baseline Surface Radiation Network (BSRN/WCRP): New Precision  
635 Radiometry for Climate Research, *Bull. Am. Meteorol. Soc.*, , *79*, 2115–2136.

636 Prata, A. J. (1996), A new long-wave formula for estimating downward clear-sky radiation at  
637 the surface, *Q. J. R. Meteorol. Soc.*, , *122*, 1127–1151, doi:10.1256/smsqj.53305.

638 Ritter, C., J. Notholt, J. Fischer, and C. Rathke (2005), Direct thermal radiative forcing of  
639 tropospheric aerosol in the Arctic measured by ground based infrared spectrometry, *Geophys.*  
640 *Res. Lett.*, , *32*, 23,816-, doi:10.1029/2005GL024331.

641 Schmetz, J., P. Pili, S. Tjemkes, D. Just, J. Kerkmann, S. Rota, and A. Ratier (2002), An  
642 Introduction to Meteosat Second Generation (MSG)., *Bull. Am. Meteorol. Soc.*, , *83*, 977–992.

643 Seemann, S. W., E. E. Borbas, R. O. Knuteson, G. R. Stephenson, and H.-L. Huang (2008), De-  
644 velopment of a Global Infrared Land Surface Emissivity Database for Application to Clear Sky

- 645 Sounding Retrievals from Multispectral Satellite Radiance Measurements, *Journal of Applied*  
646 *Meteorology and Climatology*, 47, 108-, doi:10.1175/2007JAMC1590.1.
- 647 Settle, J., N. A. Bharmal, G. J. Robinson, and A. Slingo (2008), Bounding the Uncertainty of  
648 Flux Divergence Calculations in RADAGAST, *J. Geophys. Res.*, , YY, ZZ-AA, doi:10.1029/  
649 XXXYYYYZZZ.
- 650 Slingo, A., et al. (2008a), Overview of observations from the RADAGAST experiment in Niamey,  
651 Niger. Part 1: Meteorology and thermodynamic variables, *J. Geophys. Res.*, , YY, ZZ-AA,  
652 doi:10.1029/XXXYYYYZZZ.
- 653 Slingo, A., H. E. White, N. A. Bharmal, and G. J. Robinson (2008b), Overview of observations  
654 from the RADAGAST experiment in Niamey, Niger. Part 2: Radiative fluxes and divergences,  
655 *J. Geophys. Res.*, , YY, ZZ-AA, doi:10.1029/XXXYYYYZZZ.
- 656 Slingo, A., et al. (2006), Observations of the impact of a major Saharan dust storm on the  
657 atmospheric radiation balance, *Geophys. Res. Lett.*, , 33, 24,817-, doi:10.1029/2006GL027869.
- 658 Soden, B. J., D. D. Turner, B. M. Lesht, and L. M. Miloshevich (2004), An analysis of satellite,  
659 radiosonde, and lidar observations of upper tropospheric water vapor from the Atmospheric  
660 Radiation Measurement Program, *J. Geophys. Res.*, , 109, 4105-, doi:10.1029/2003JD003828.
- 661 Turner, D. D. (2008), Ground-based retrievals of optical depth, effective radius, and composition  
662 of airborne mineral dust above the Sahel, *J. Geophys. Res. Atmos.*, YY, ZZ-AA, doi:10.1029/  
663 XXXYYYYZZZ.
- 664 Turner, D. D., S. A. Clough, J. C. Liljegren, E. E. Clothiaux, K. E. Cady-Pereira, and K. L.  
665 Gaustad (2007), Retrieving Liquid Water Path and Precipitable Water Vapor From the At-  
666 mospheric Radiation Measurement (ARM) Microwave Radiometers, *IEEE Transactions on*  
667 *Geoscience and Remote Sensing*, 45, 3680–3690, doi:10.1109/TGRS.2007.903703.

- 668 Wan, Z., and Z.-L. Li (1997), A physics-based algorithm for retrieving land-surface emissivity and  
669 temperature from EOS/MODIS data, *IEEE Transactions on Geoscience and Remote Sensing*,  
670 *35*, 980–996, doi:10.1109/36.602541.
- 671 Wang, K., Z. Wan, P. Wang, M. Sparrow, J. Liu, X. Zhou, and S. Haginoya (2005), Estimation  
672 of surface long wave radiation and broadband emissivity using Moderate Resolution Imaging  
673 Spectroradiometer (MODIS) land surface temperature/emissivity products, *J. Geophys. Res.*,  
674 *110*, 11,109-, doi:10.1029/2004JD005566.
- 675 WMO/TD-No. 411 (1990), Global climate modelling, *Tech. rep.*, WMO, Geneva, Switzerland.

**Table 1.** Surface data-streams used in this work. These are either measurements from the AMF deployment to Niamey or derived thereof.

Data-stream	Variables measured	Temporal resolution
aerisummary	averaged longwave zenith-pointing spectrally-resolved radiance	400 s
skyrad60s	downwelling longwave flux, sky-looking infra-red thermometer ( <code>down_long_hemisp_shaded2</code> variable is used for flux.)	60 s
gndrad60s	upwelling longwave flux, surface-looking infra-red thermometer	60 s
mwrret	Improved microwave radiometer column water vapor retrievals	60 s
sondownpn	Rawinsonde, Vaisala RS-92, ascents	4 daily
met	2 m height temperature, pressure	60 s

**Table 2.** Satellite data-streams used in this work.

Name	Description	Spatial resolution
GERB ARG	Edition 1 radiances and fluxes	$\sim 46 \times 46$ km
GERB SHI	Radiances and fluxes from GERB+SEVIRI	$\sim 9 \times 9$ km
NWCSAF cloud mask	SEVIRI-based cloud mask	$\sim 3 \times 3$ km
MOD11A2/MYD11A2	Surface temperature from MODIS Terra/Aqua	$1 \times 1$ km
CIMMS IR emissivity	Surface LW emissivity via MODIS measurements	$0.05^\circ \times 0.05^\circ$

**Table 3.** ES96 band-passes used for comparison with AERI radiances. The parentheses represent subsidiary sources of emission, either because they are well determined or relatively unimportant.

<i>hadgem1_3</i> band number	Bandpass		Emission sources
	cm <sup>-1</sup>	microns	
4	590–750	13.3–17.0	CO <sub>2</sub> , H <sub>2</sub> O, (O <sub>3</sub> )
5	800–990 & 1120–1200	8.3–8.9 & 10.1–12.5	H <sub>2</sub> O, aerosol, CO <sub>2</sub> , (N <sub>2</sub> O, O <sub>3</sub> )
8	1330–1500	6.7–7.5	CO <sub>2</sub> , H <sub>2</sub> O, (N <sub>2</sub> O, CH <sub>4</sub> )

**Table 4.** Parameters to the fits shown in figure 8, of the form  $\Delta(F) = \alpha + \beta \bar{\tau} / (1 + \bar{\tau})$ , where  $\Delta(F)$  is obs-calc for the diurnal-mean DLR and  $\langle \tau \rangle$  is diurnal-mean AOT(1020 nm).

CWV range		$\alpha / \text{Wm}^{-2}$	$\beta / \text{Wm}^{-2}$
lower / cm	upper /cm		
0	1	$0.7 \pm 1.6$	$96.3 \pm 5.9$
1	1.5	$4.1 \pm 1.5$	$73.5 \pm 5.6$
1.5	2.5	$5.2 \pm 1.4$	$53.2 \pm 5.9$
2.5	$\infty$	$6.6 \pm 2.7$	$22.4 \pm 9.7$

**Table 5.** Obs-calc,  $\Delta(L) = L_{obs} - L_{calc}$ , for TOA radiances. The calculated radiances are from ES96 simulations and observed from GERB ARG measurements (as medians and inter-quartile range). Values are shown for use of unscaled & scaled LST. The associated percentage differences are also shown.

Hour bin	$\Delta(L) / \text{Wm}^{-2}\text{sr}^{-1}$		$(\Delta_{IRT} - \Delta_s) / \Delta_{IRT}$ / %-age
	via IRT LST $\Delta_{IRT}$	via scaled LST $\Delta_s$	
All	$-4.3^{+1.4}_{-2.1}$	$-4.5^{+1.4}_{-1.9}$	$-1.8^{+11.3}_{-10.1}$
06 UT	$-3.2^{+0.4}_{-1.4}$	$-2.8^{+0.5}_{-1.2}$	$11.6^{+10.2}_{-7.0}$
11 UT	$-5.8^{+2.1}_{-2.0}$	$-5.7^{+1.6}_{-2.0}$	$-7.8^{+7.9}_{-10.8}$
17 UT	$-4.0^{+1.0}_{-1.7}$	$-4.6^{+1.3}_{-1.4}$	$-4.5^{+3.6}_{-10.7}$
23 UT	$-3.4^{+0.9}_{-0.6}$	$-3.1^{+1.0}_{-0.8}$	$9.6^{+16.3}_{-6.3}$

**Table 6.** Obs-calc,  $\Delta(V) = V_{obs} - V_{calc}$  results for the GERB ARG TOA pristine radiances,  $L$ , and fluxes,  $F$ , per time bin (as medians and inter-quartile range). The data are shown for the whole year, and subdivided into the two primary seasons. The dash denotes when the number of data points for that time was fewer than 10% of the total number for that day.

Season	Time	$\Delta$	
		$L / \text{Wm}^{-2}\text{sr}^{-1}$	$F / \text{Wm}^{-2}$
Both	All	$-4.4^{+1.4}_{-1.9}$	$-12.0^{+3.2}_{-4.7}$
	06 UT	$-2.8^{+0.5}_{-1.9}$	$-10.4^{+1.7}_{-4.1}$
	11 UT	$-5.7^{+1.7}_{-2.0}$	$-14.1^{+5.0}_{-5.6}$
	17 UT	$-4.6^{+1.3}_{-1.4}$	$-13.0^{+2.9}_{-3.7}$
	23 UT	$-2.8^{+0.9}_{-1.0}$	$-9.8^{+2.1}_{-2.7}$
Dry	All	$-3.7^{+1.3}_{-2.3}$	$-10.8^{+2.7}_{-5.8}$
	06 UT	$-2.4^{+0.5}_{-0.6}$	$-9.5^{+1.1}_{-1.5}$
	11 UT	$-5.3^{+1.5}_{-2.4}$	$-12.9^{+4.1}_{-7.4}$
	17 UT	$-3.5^{+1.3}_{-3.0}$	$-12.0^{+3.3}_{-7.0}$
	23 UT	$-2.1^{+0.4}_{-1.0}$	$-8.4^{+1.1}_{-3.0}$
Wet	All	$-5.1^{+1.1}_{-1.4}$	$-13.4^{+2.8}_{-3.3}$
	06 UT	-	-
	11 UT	$-6.4^{+1.3}_{-1.3}$	$-14.3^{+3.8}_{-3.7}$
	17 UT	$-4.9^{+0.9}_{-0.9}$	$-13.3^{+2.7}_{-3.0}$
	23 UT	$-3.9^{+0.6}_{-0.9}$	$-12.1^{+1.7}_{-2.5}$

**Table 7.** Obs-calc,  $\Delta(V) = V_{obs} - V_{calc}$  results for the GERB ARG TOA clear sky radiances,  $L$ , and fluxes,  $F$ , per time bin (as medians and inter-quartile range). The data are shown for the whole year, and subdivided into the two primary seasons. The dash denotes when the number of data points for that time was fewer than 10% of the total number for that day.

Season	Time	$\Delta$	
		$L / \text{Wm}^{-2}\text{sr}^{-1}$	$F / \text{Wm}^{-2}$
Both	All	$-3.0^{+1.1}_{-1.7}$	$-6.6^{+5.8}_{-3.9}$
	06 UT	$-2.7^{+0.3}_{-2.0}$	$-9.3^{+1.8}_{-3.8}$
	11 UT	$-3.3^{+1.3}_{-2.0}$	$-2.3^{+3.8}_{-6.0}$
	17 UT	$-3.6^{+1.4}_{-1.3}$	$-8.2^{+4.5}_{-3.5}$
	23 UT	$-2.4^{+0.5}_{-1.1}$	$-7.5^{+1.7}_{-2.9}$
Dry	All	$-2.4^{+0.7}_{-1.3}$	$-5.1^{+6.0}_{-3.5}$
	06 UT	$-2.4^{+0.4}_{-0.6}$	$-8.6^{+1.6}_{-1.7}$
	11 UT	$-2.5^{+0.9}_{-1.7}$	$-0.3^{+2.6}_{-5.3}$
	17 UT	$-2.5^{+1.0}_{-1.9}$	$-4.8^{+3.5}_{-3.7}$
	23 UT	$-2.1^{+0.4}_{-0.9}$	$-7.0^{+1.8}_{-3.0}$
Wet	All	$-4.2^{+1.1}_{-1.4}$	$-9.3^{+4.8}_{-5.0}$
	06 UT	-	-
	11 UT	$-4.5^{+1.4}_{-2.2}$	$-6.3^{+3.6}_{-6.9}$
	17 UT	$-4.1^{+1.1}_{-0.9}$	$-9.9^{+3.5}_{-4.2}$
	23 UT	$-3.5^{+0.6}_{-1.2}$	$-9.5^{+2.5}_{-3.1}$

**Table 8.** Summary of the LW flux components available for divergence calculations. The bold entries denote those which are considered the best estimate (least biased and/or most accurate).

Flux	Sources	Comment
Surface down, $F_{DLR}$	<b>AMF</b> ES96 (clear sky)	(defined equivalent to AMF)
Surface up, $F_{ULR}$	AMF <b>ES96</b>	biased w.r.t GERB ARG area unbiased w.r.t GERB ARG area
TOA up, $F_{OLR}$	GERB ARG Edition 1 ES96 (clear sky) <b>GERB/ES96 hybrid</b>	from aerosol-free $R$ using simple aerosol representation GERB radiances and ES96 $R$

**Table 9.** Atmospheric LW divergences for each time bin through 2006, from the three flux component collections (as medians and inter-quartile range).

Flux collection	Divergence / $\text{Wm}^{-2}$			
	06 UT	11 UT	17 UT	23 UT
Observations	$-194.7^{+6.6}_{-17.9}$	$-110.1^{+11.8}_{-13.8}$	$-188.3^{+10.7}_{-8.5}$	$-198.6^{+8.3}_{-14.3}$
Simulations	$-207.2^{+6.3}_{-19.3}$	$-117.8^{+8.8}_{-12.6}$	$-199.7^{+9.3}_{-9.4}$	$-208.6^{+5.8}_{-16.3}$
Best estimate	$-198.2^{+5.9}_{-12.4}$	$-108.6^{+11.9}_{-11.4}$	$-189.3^{+9.8}_{-6.6}$	$-203.0^{+9.2}_{-10.8}$

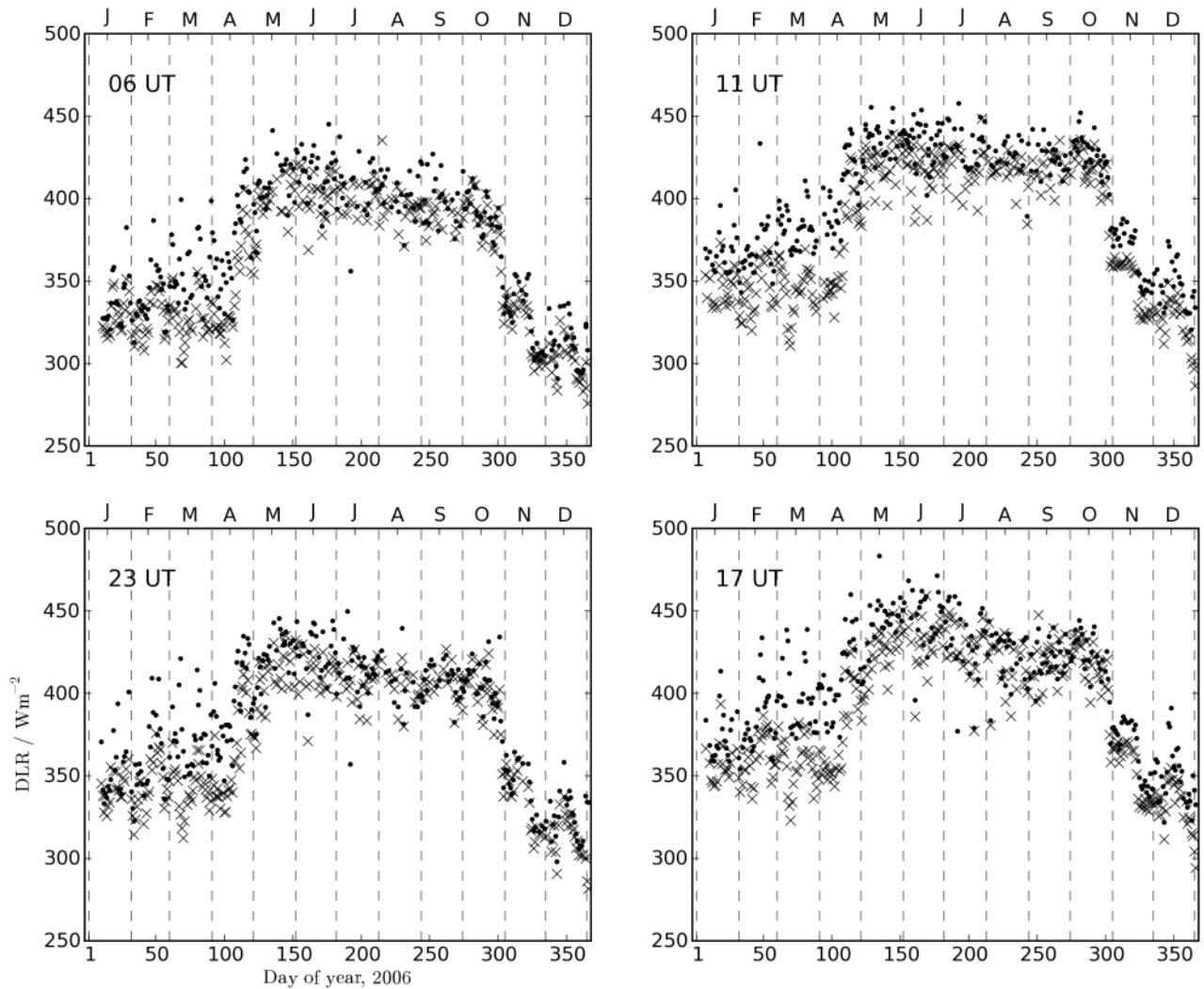


**Figure 1.** The flux measurements (points) with simulations (crosses): surface downwelling radiation (DLR). The boxes run clockwise in time; 06 UT, 11 UT, 17 UT, and 23 UT.

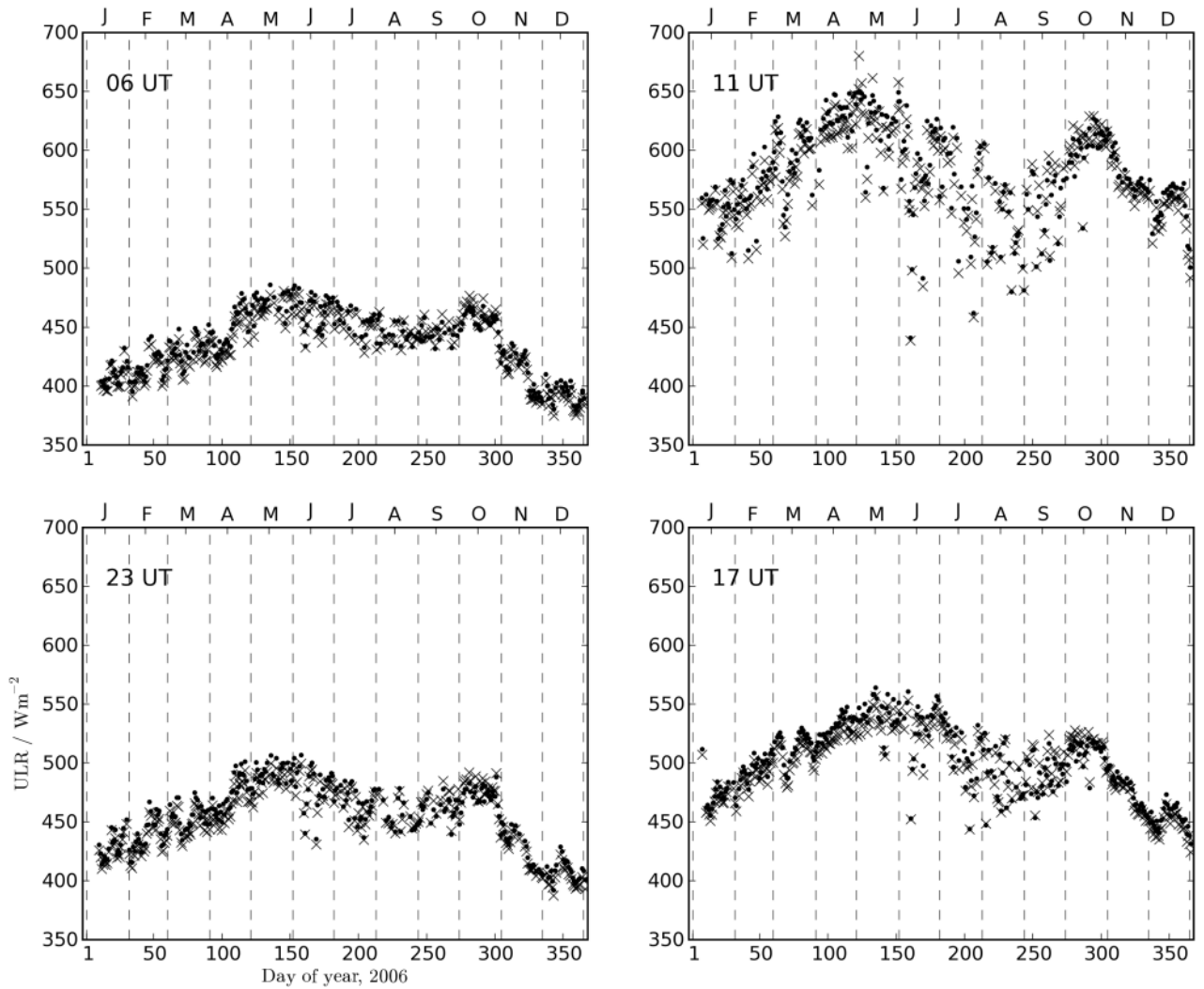


**Figure 2.** The flux measurements (points) with simulations (crosses): surface upwelling radiation (ULR). The boxes run clockwise in time; 06 UT, 11 UT, 17 UT, and 23 UT.

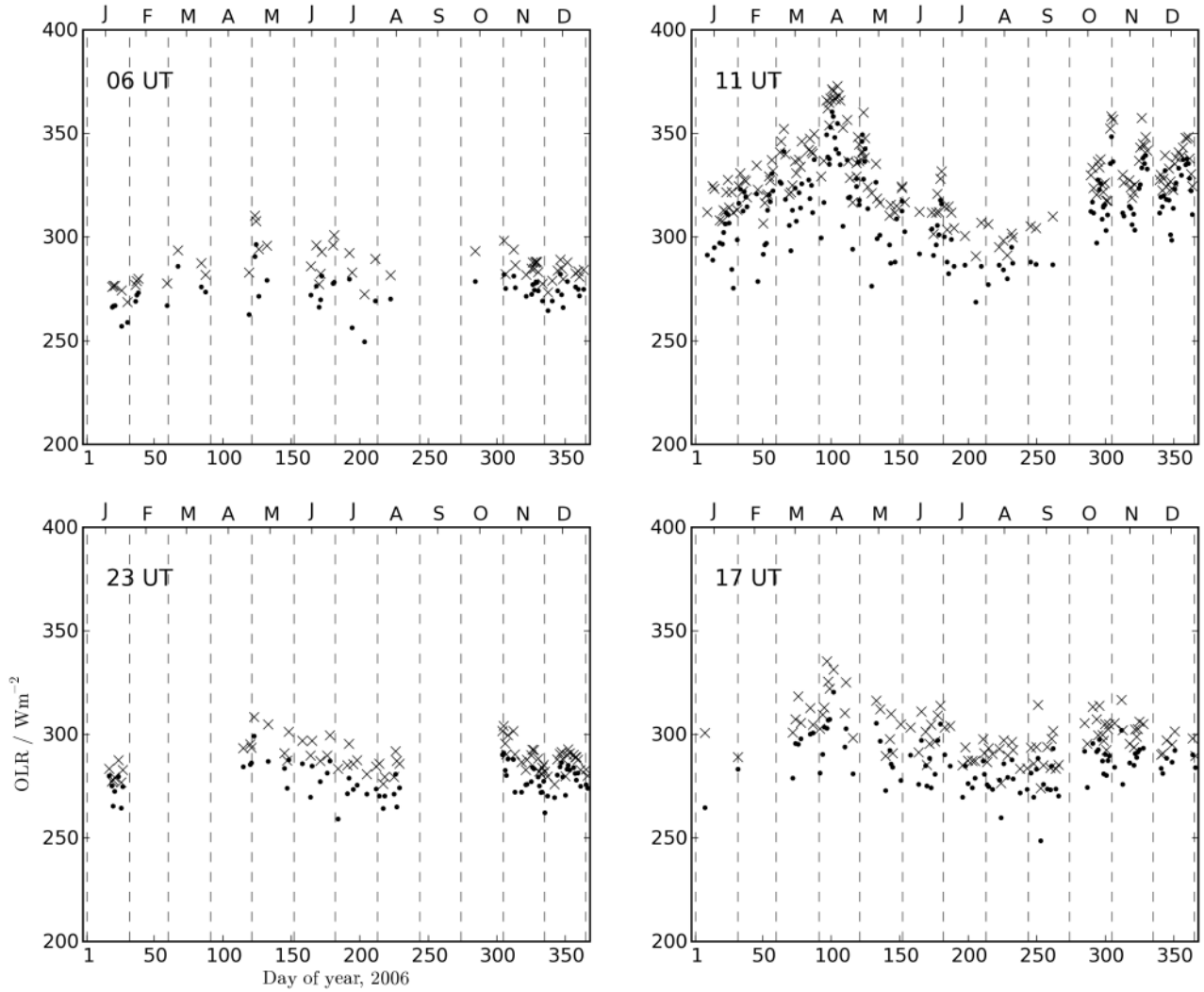


**Figure 3.** The flux measurements (points) with simulations (crosses): outgoing radiation (OLR). The boxes run clockwise in time; 06 UT, 11 UT, 17 UT, and 23 UT. The relative paucity for the 23 UT time is due to GERB sun-avoidance operations.

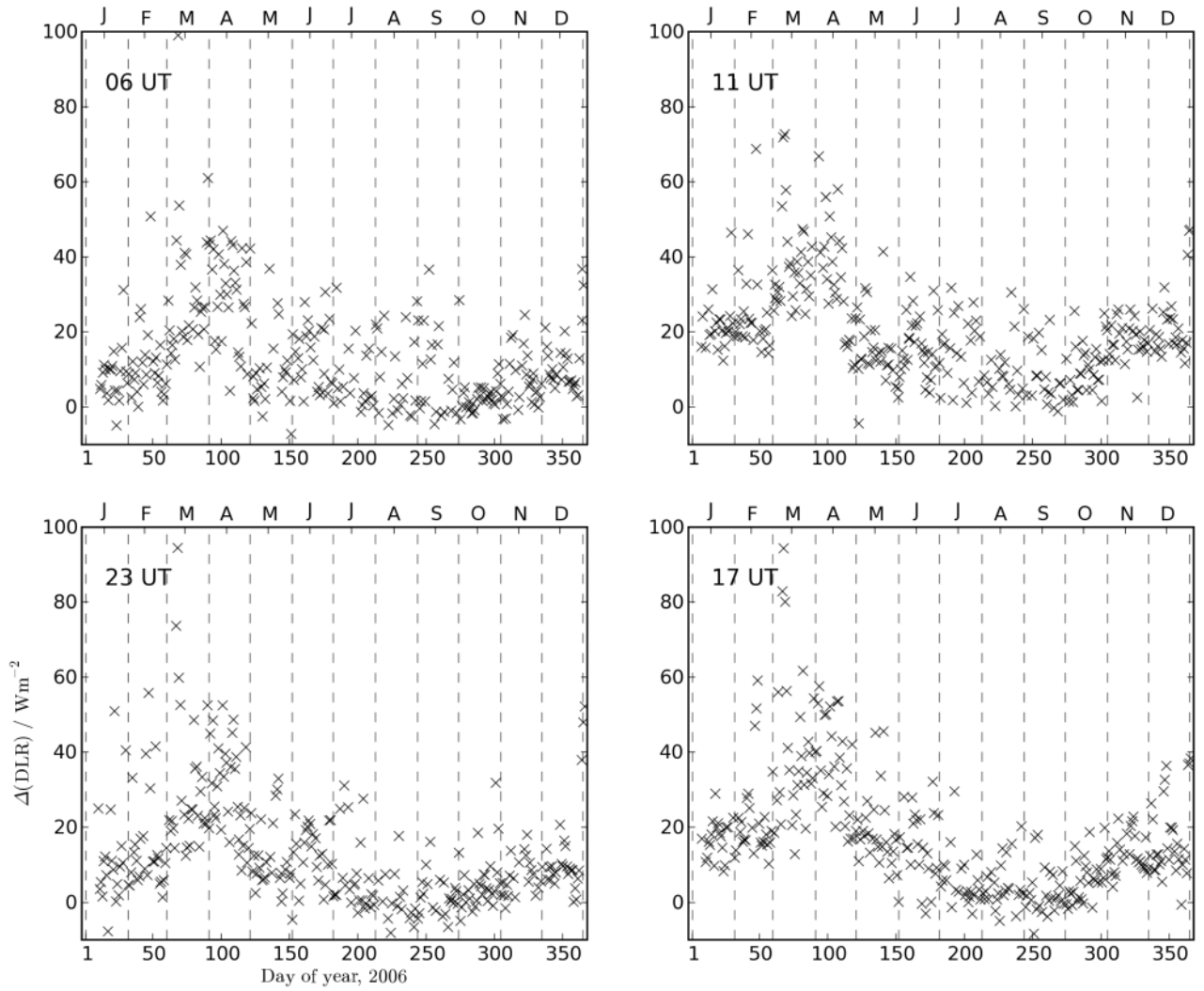


**Figure 4.** The difference between measurements and calculations, c.f. figure 1: downwelling radiation (DLR). The boxes run clockwise in time; 06 UT, 11 UT, 17 UT, and 23 UT.

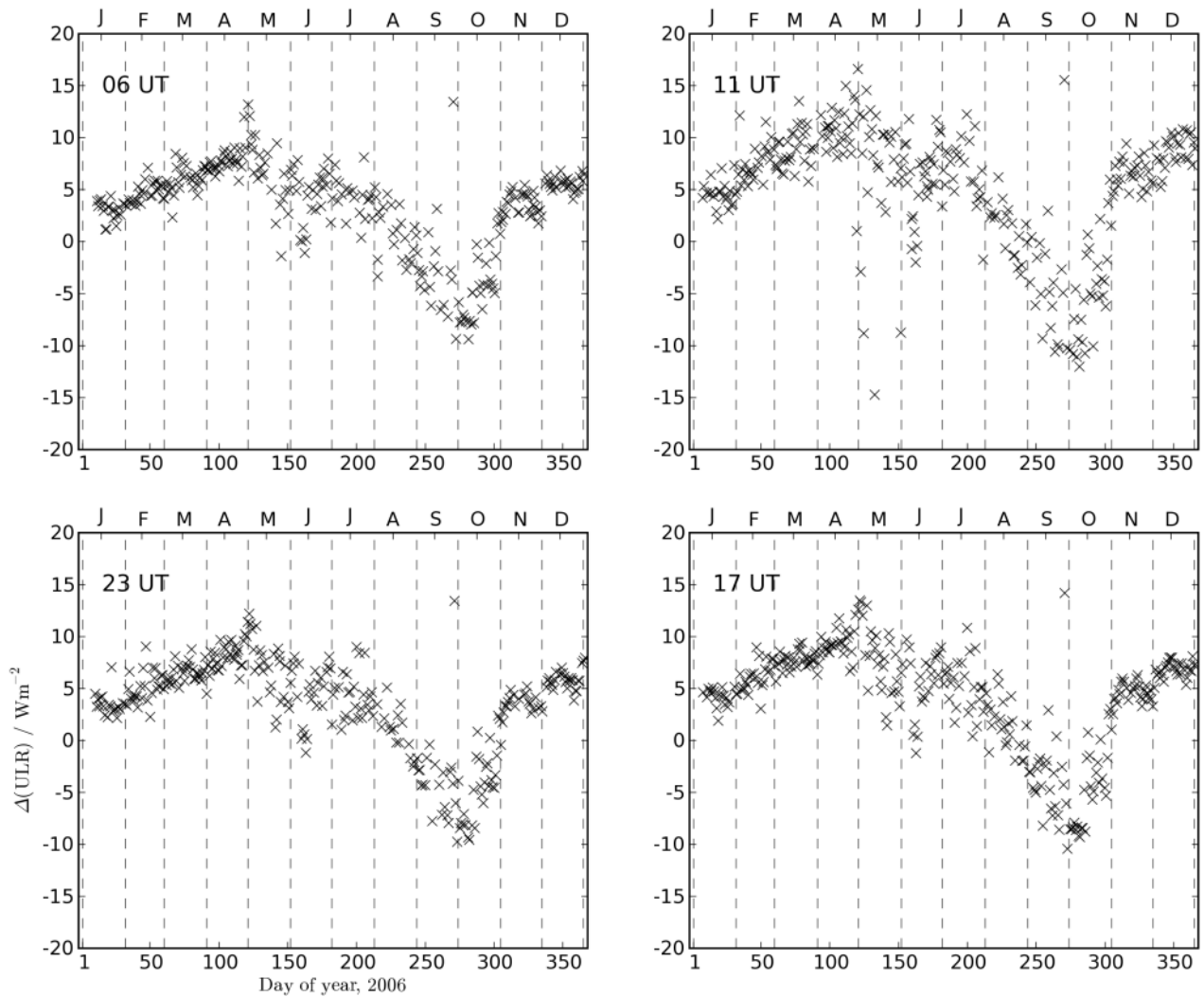


**Figure 5.** The difference between measurements and calculations, c.f. figure 2: surface upwelling radiation (ULR). The boxes run clockwise in time; 06 UT, 11 UT, 17 UT, and 23 UT.

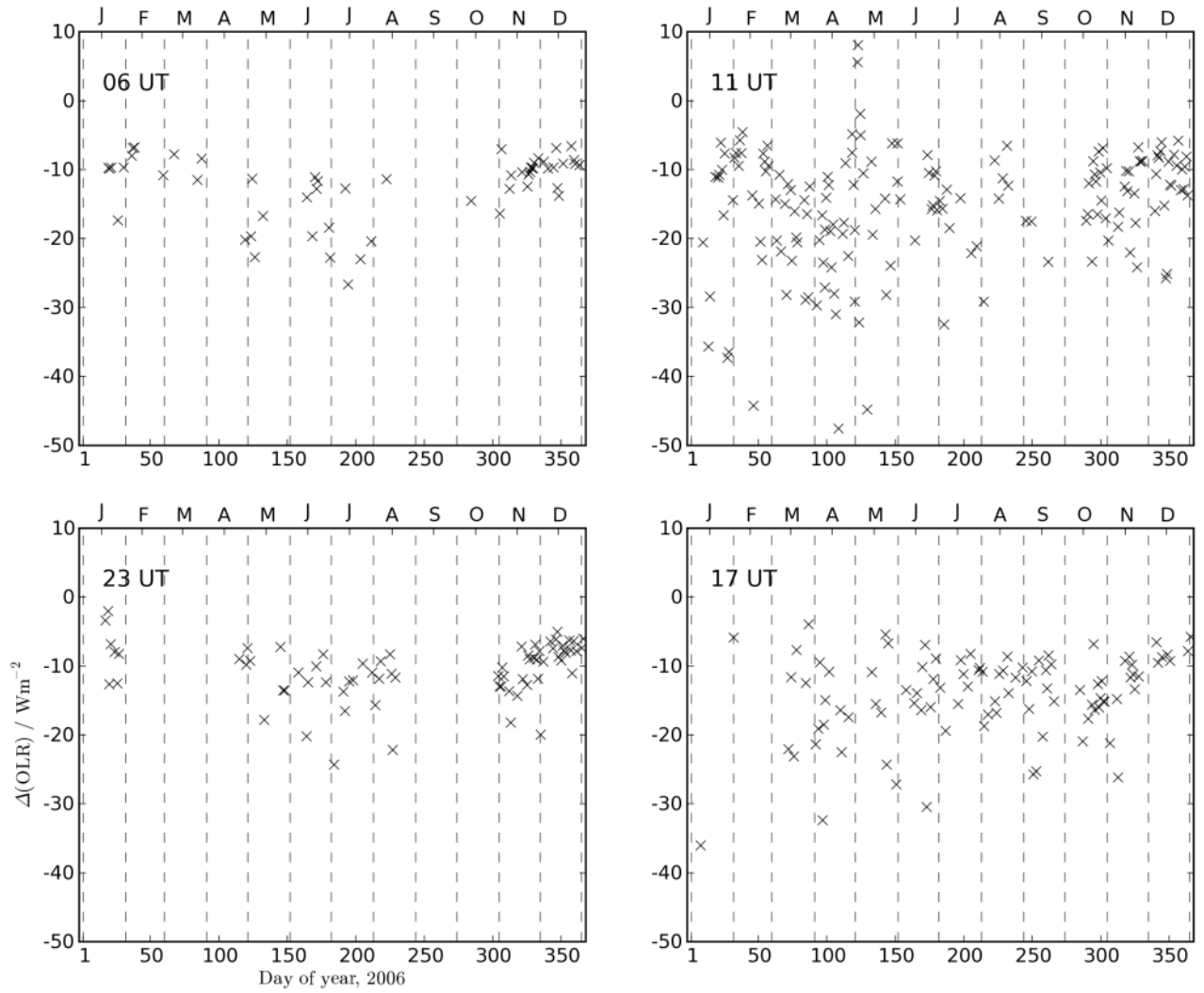


**Figure 6.** The difference between measurements and calculations, c.f. figure 3: outgoing radiation (OLR). The boxes run clockwise in time; 06 UT, 11 UT, 17 UT, and 23 UT.

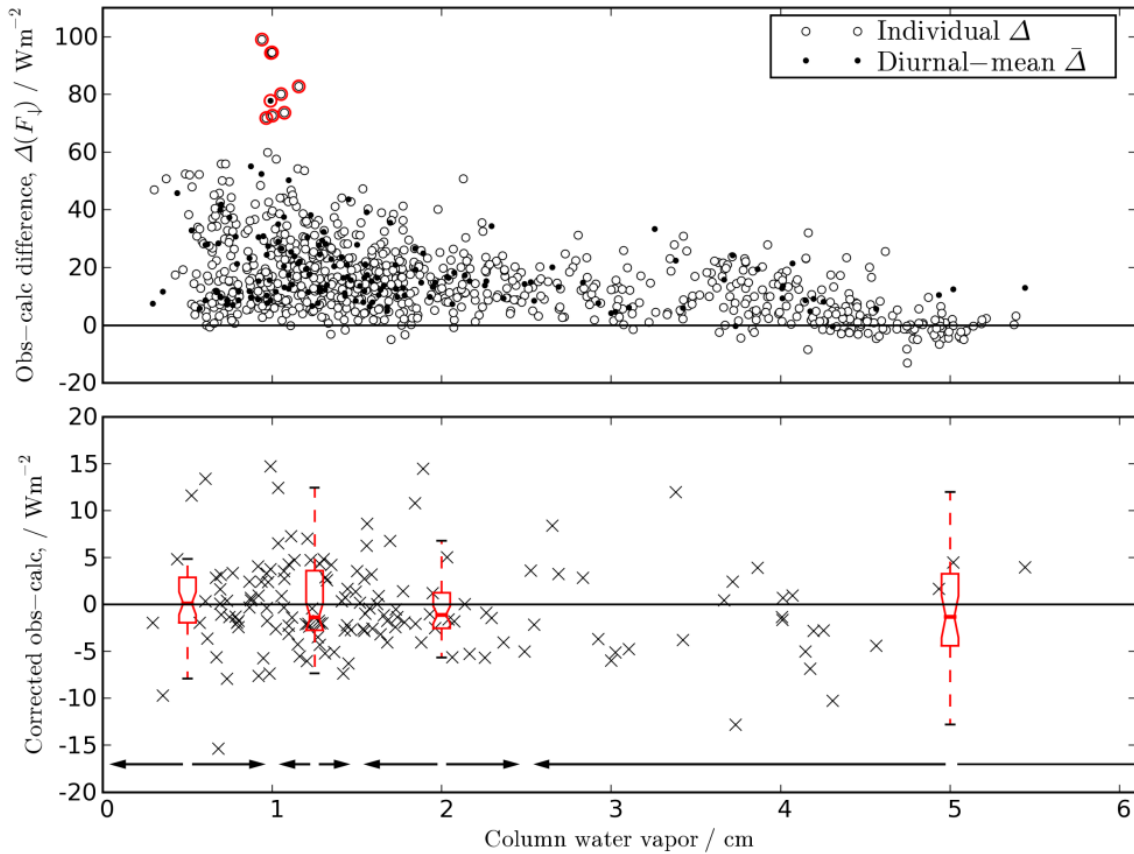


**Figure 7.** *Upper panel:* Observation-calculation (obs-calc) of DLR (from individual calculations,  $\Delta$ , and diurnal-means,  $\bar{\Delta}$ ) vs. CWV; red highlights show the effect of the March dust storm. *Lower panel:* The same but when the ‘correction’ for the direct effect c.f. figure 8 is included. The box-whisker plot shows the statistics of the ‘corrected’ obs-calc differences for each CWV bin, denoted by the arrows.

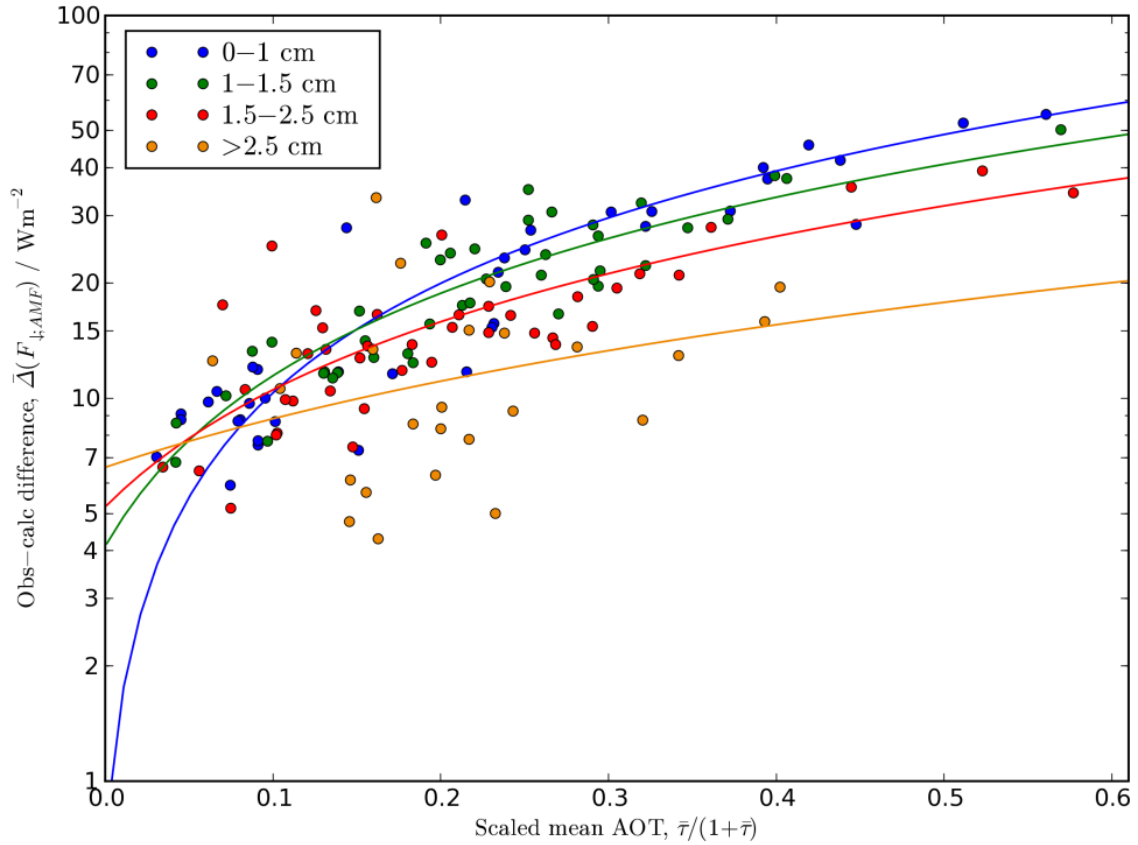


**Figure 8.** Observation-calculation (obs-calc) of diurnal-mean DLR,  $\bar{\Delta}$ , vs. the scaled, diurnal-mean AOT(1020 nm),  $\bar{\tau}$ . The data are divided into four CWV bins, and the parameters for the associated linear fits are listed in table 4. These fits are used in figure 7 to ‘correct’ for the aerosol direct effect.

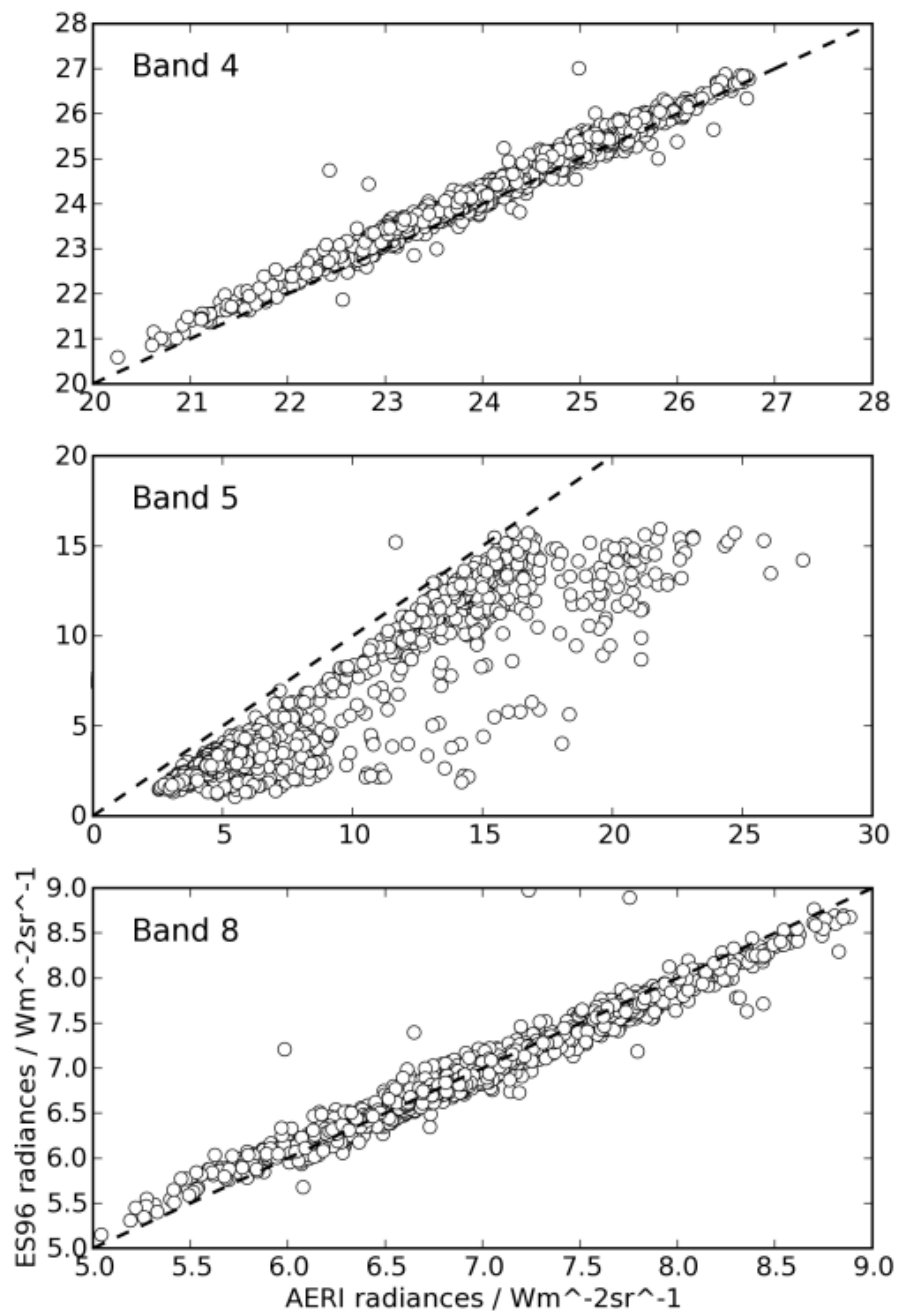


**Figure 9.** Comparison of AERI radiances in bands 4, 5, & 8 (c.f. table 3 for the band-passes) for pristine (aerosol free) RT calculations.

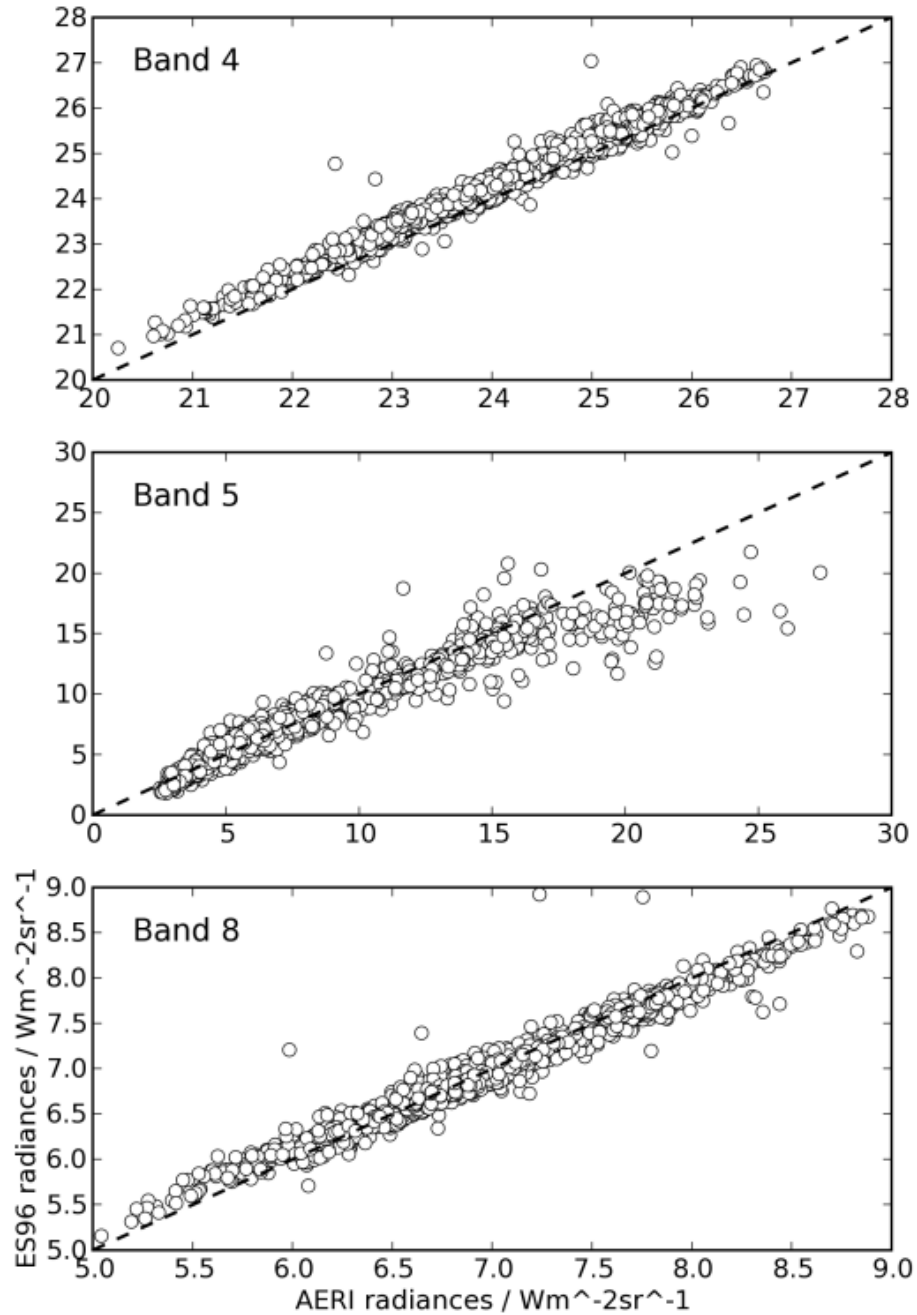


**Figure 10.** Comparison of AERI radiances in ES96 bands 4, 5, & 8 (c.f. table 3 for the band-passes) for clear sky (aerosol included) simulations.

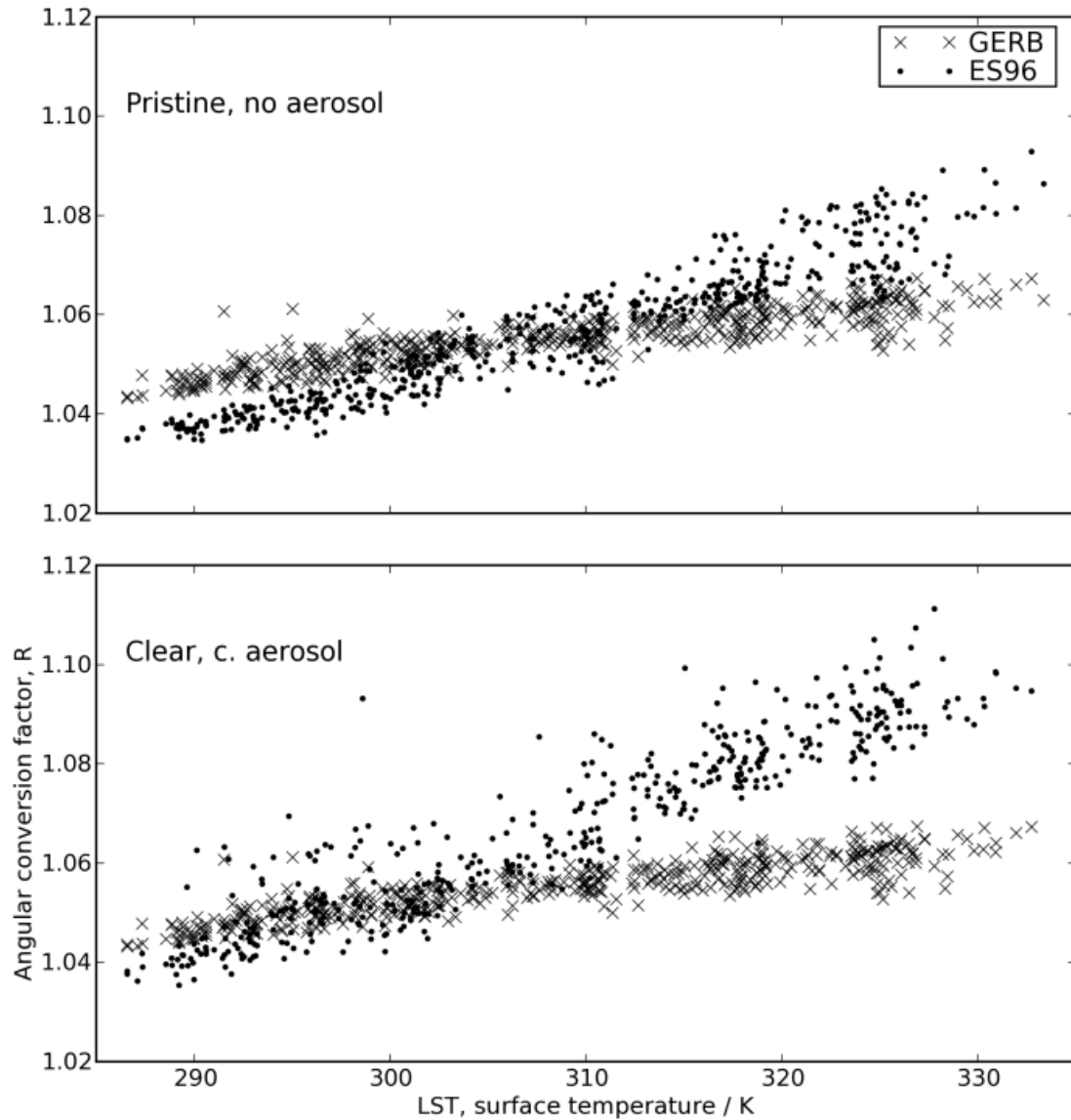


**Figure 11.** *Upper panel:* The angular conversion factor,  $R$ , from radiance to flux. The points show the values derived from ES96 calculations and the crosses contemporaneous values from GERB observations (thus crosses are equivalent between panels). *Lower panel:* As above, but for clear sky conditions.

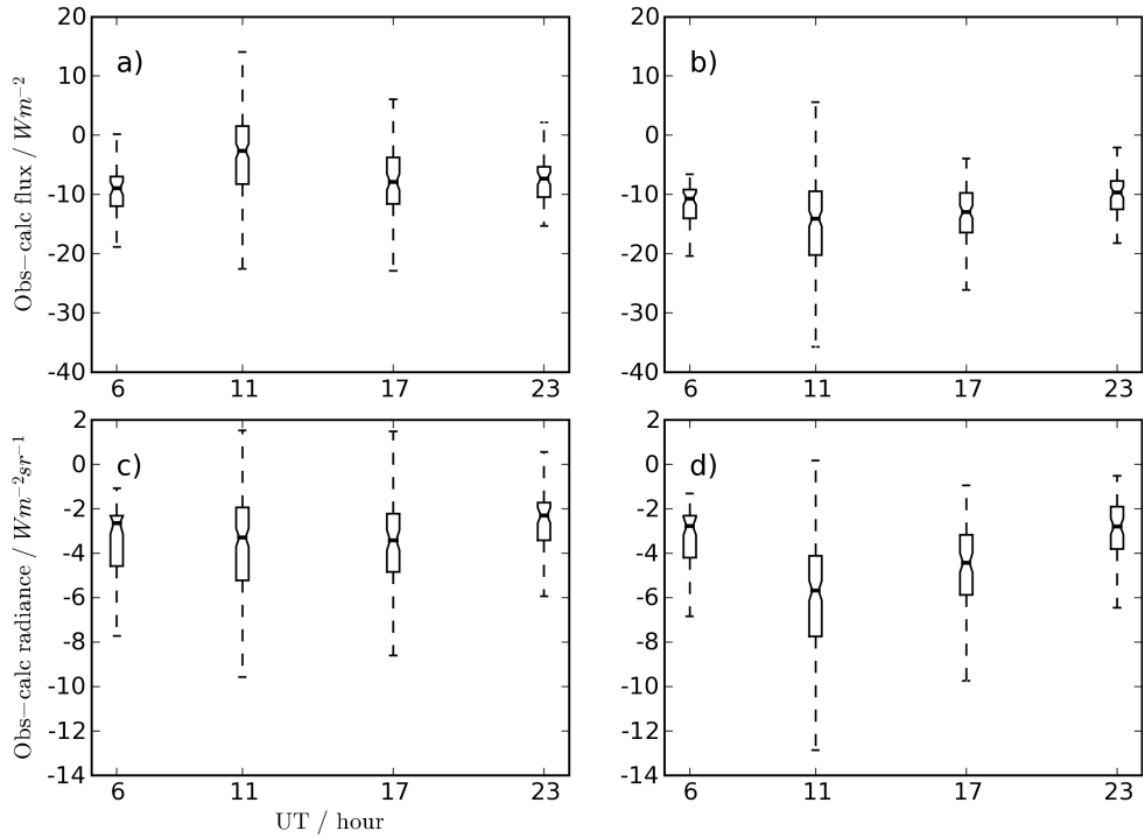


**Figure 12.** Observation-calculation (obs-calc) difference for radiances and fluxes. Panels a) and b) represent fluxes, with and without aerosol. Panels c) and d) are the equivalent for radiances. The boxes represent the inter-quartile range, the solid bar & notch the median, and the whiskers data within 150% of the upper and lower quartiles.

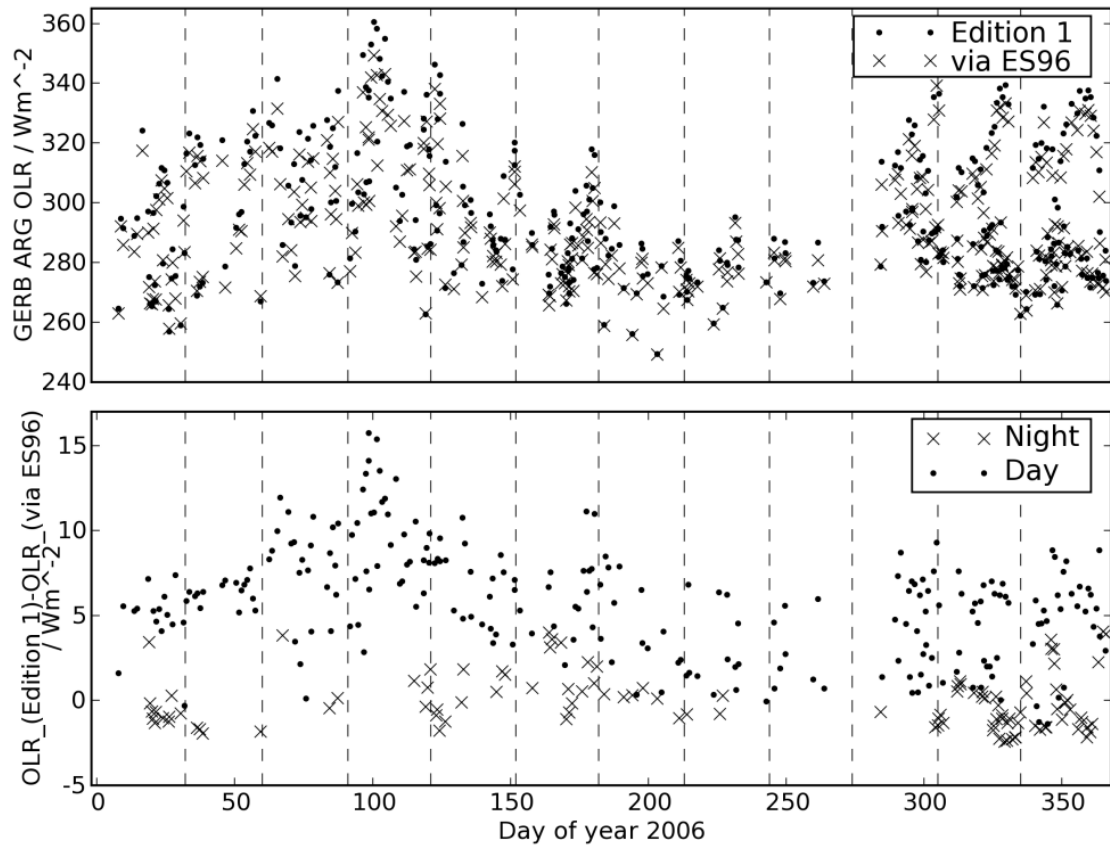


**Figure 13.** *Upper panel:* The GERB ARG Edition 1 flux and the hybrid GERB/ES96 flux as a time series. *Lower panel:* The difference between the two time series.

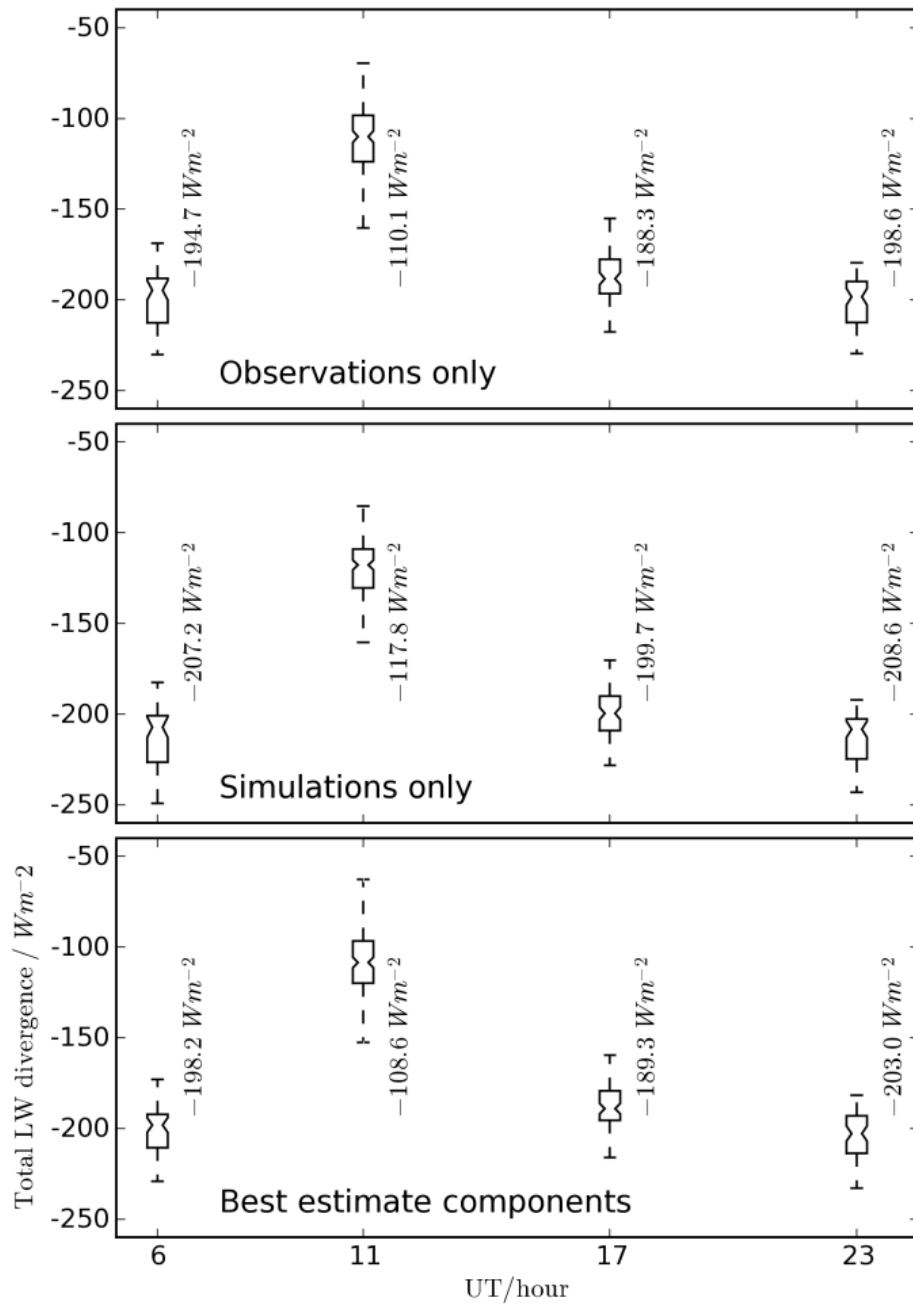


**Figure 14.** The atmospheric divergence calculated from GERB & AMF observations (top), simulation fluxes (middle) and best estimate flux components (bottom). The quoted values correspond to the median (notch) for each time bin.